The young pulsar PSR B0540-69.3 and its synchrotron nebula in the optical and X-rays[*]

N. I. Serafimovich[1,2], Yu. A. Shibanov[1], P. Lundqvist[2], and J. Sollerman[2]

[1] Ioffe Physical Technical Institute, Politekhnicheskaya 26, St. Petersburg, 194021, Russia
[2] Stockholm Observatory, AlbaNova Science Center, Department of Astronomy, SE-106 91 Stockholm, Sweden

Abstract. The young PSR B0540-69.3 in the LMC is the only pulsar (except the Crab pulsar) for which a near-UV spectrum has been obtained. However, the absolute flux and spectral index of the HST/FOS spectrum are significantly higher than suggested by previous broad-band time-resolved groundbased UBVRI photometry. To investigate this difference, observations with ESO/VLT/FORS1 and analysis of HST/WFPC2 archival data were done. We show that the HST and VLT spectral data for the pulsar have $\gtrsim 50\%$ nebular contamination and that this is the reason for the above mentioned difference. The broadband HST spectrum for the range 3300–8000 Å is clearly nonthermal and has a negative spectral index, $F_\nu \propto \nu^{-\alpha}$ with $\alpha_\nu = 1.07^{+0.20}_{-0.19}$. This is different from the almost flat spectrum of the Crab pulsar, and also steeper than for the previously published broadband photometry of PSR B0540-69.3. We have also studied the spatial variations of the brightness and spectral index of the Pulsar Wind Nebula (PWN) around the pulsar, and find no significant spectral index variation over the PWN. The HST data show a clear asymmetry of the surface brightness distribution along the major axis of the torus-like structure of the PWN with respect to the pulsar position, also seen in Chandra/HRC X-ray images. This is different from the Crab PWN and likely linked to the asymmetry of the surrounding SN ejecta. The HST/WFPC2 archival data have an epoch separation by 4 years, and this allows us to estimate the proper motion of the pulsar. We find a motion of 4.9 ± 2.3 mas yr^{-1} (corresponding to a transverse velocity of 1190 ± 560 km s^{-1}) along the southern jet of the PWN. If this is confirmed at a higher significance level by future observations, this makes PSR B0540-69.3 the third pulsar with a proper motion aligned with the jet axis of its PWN, which poses constraints on pulsar kick models. To establish the multiwavelength spectrum of the pulsar and its PWN, we have included recent Chandra X-ray data, and discuss the soft pulsar X-ray spectrum based on spectral fits including absorption by interstellar gas in the Milky Way, LMC as well as the supernova ejecta. We have compared the multiwavelength spectra of PSR B0540-69.3 and the Crab pulsar, and find that both PSR B0540-69.3 and the Crab pulsar have a weaker flux in the optical than suggested by a low-energy power-law extension of the X-ray spectrum. This optical depression is more severe for PSR B0540-69.3 than for the Crab pulsar. The same trend is seen for the PWNe of the two pulsars, and continues for low energies also out in the radio band. We discuss possible interpretations of this behavior.

Key words. pulsars: individual: PSR B0540-69.3 – ISM: supernova remnants – supernovae: general – Astrometry

1. Introduction

PSR B0540-69.3 in the Large Magellanic Cloud (LMC) was discovered as a pulsed ($P = 50.2$ ms) X-ray source by Seward et al. (1984). Pulsations have since also been detected in the optical and at radio wavelengths (Middleditch & Pennypacker 1985; Manchester et al. 1993a). The pulse profile in the optical (Boyd et al. 1995) is broad and double-peaked, with a sep-

aration of ~ 0.2 in phase between the two maxima, consistent with what is also seen in X-rays (Seward et al. 1984; de Plaa et al. 2003). The profile is also broad in the radio (the duty cycle is $\gtrsim 80\%$), and there is a hint of a double structure (Manchester et al. 1993a).

Parameters of PSR B0540-69.3 are compiled in Table 1. The pulsar spins rapidly, is young (spin down age 1660 yr), and sits in a compact synchrotron nebula (see Fig. 1), which we will henceforth refer to as its pulsar wind nebula (PWN). The similarities with the Crab pulsar and its nebula are such that PSR B0540-69.3 with its supernova remnant, SNR 0540-69.3, are sometimes referred to as the "Crab twin". Even the structures of the

Table 1. Parameters of PSR B0540-69.3 (Manchester et al. 1993a, unless specified otherwise).

Observed					Derived			
P	$\dot{P}$	μ^a	$l,\,b^b$	DM^c	τ^d	B^e	$\dot{E}$	d^f
ms	10^{-15}	mas yr^{-1}		cm^{-3} pc	yr	G	erg s^{-1}	kpc
50.2	479.04 ± 0.10	~ 5	$279°\!.7$ $-31°\!.5$	146 ± 4	1660	4.96×10^{12}	1.495×10^{38}	51 ± 1.3

[a] Indirect proper motion estimates (Manchester et al. 1993b)
[b] Galactic coordinates (Kaaret et al. 2001)
[c] Dispersion measure
[d] Spin-down age $P/2\dot{P}$
[e] Magnetic field for a 10 km radius NS $3.2 \times 10^{19}(P\dot{P})^{1/2}$
[f] Distance to the LMC (Panagia 2004)

PWNe appear to be similar. Both have a torus and jets (Gotthelf & Wang 2000), although the proper motion for PSR B0540-69.3, suggested by Manchester et al. (1993b) based on a displacement between the pulsar optical position and the center of the PWN as seen in radio, seems not to be along the spin axis as it is in the Crab case.

There are, however, differences on a larger scale. While the PWN of PSR B0540-69.3 is surrounded by an X-ray and radio emitting outer shell of radius $\sim 30''$, or ~ 7.3 pc (Manchester et al. 1993b; Gotthelf & Wang 2000), an outer shell around the Crab is still not confirmed (although high-velocity gas has been revealed in the UV, Sollerman et al. 2000). Another difference is that SNR 0540-69.3 is oxygen-rich (e.g., Kirshner et al. 1989; Serafimovich et al. 2004), whereas the Crab Nebula has nearly normal solar abundances of metals (Blair et al. 1992 and references therein). It is therefore believed that the progenitor to PSR B0540-69.3 was a much more massive star than the Crab progenitor (Kirshner et al. 1989).

PSR B0540-69.3 is one of few pulsars for which a near-UV or optical spectrum has been reported. Hill et al. (1997) obtained a time-integrated near-UV spectrum with HST/FOS and Middleditch & Pennypacker (1985) used time-resolved photometry to establish a broadband ground-based UBVRI spectrum in the optical. These two spectra show, however, a significant difference in absolute flux in the spectral range where they overlap. To investigate this mismatch we have added two recent sets of data, one is the ESO/VLT/FORS spectroscopy of SNR 0540-69.3 analyzed by Serafimovich et al. (2004), and the other is HST/WFPC2 imaging (Caraveo et al. 2000; Morse 2003) retrieved from the HST archive. A bonus of our study is that we also obtain the optical spectrum of the PWN around PSR B0540-69.3. This was first studied quantitatively by Chanan et al. (1984), albeit at a low spatial resolution which did not allow them to resolve the pulsar from the PWN.

To connect the optical pulsar emission to the emission at other wavelengths, we have also included recent results from radio and X-rays. Previous attempts to establish the multiwavelength spectrum of PSR B0540-69.3 have assumed a rather high hydrogen column density for the X-ray absorption, $N_{\rm H} \sim 4.6 \times 10^{21}$ cm^{-2} (Kaaret et al. 2001). With this value for $N_{\rm H}$ it is possible to fit the soft

X-ray spectrum with a single power-law. This suggests a non-thermal nature of the emission, likely to be formed in the magnetosphere of the rotating neutron star (NS). There are, however, reasons to reinvestigate this since the spectral fits have not considered the fact that a large fraction of the absorbing gas has LMC abundances rather than Milky Way abundances. It could even be that the supernova ejecta can contribute to the absorption of the X-ray emission. Taking these considerations into account, we show that the situation is more complicated than assuming a single power-law for the optical/X-ray spectrum. We have also done the same exercise for the PWN.

The outline of the paper is as follows: in Sect. 2 we describe the optical spectroscopic and photometric observations of PSR B0540-69.3 and its PWN, as well as a reinvestigation of the X-ray data of Kaaret et al. (2001). In Sect. 3 we discuss these results and put them in a multiwavelength context. We also discuss results we find for the proper motion of the pulsar, and their possible interpretation.

2. Observations, data analysis and results

2.1. VLT observations and data reduction

Spectroscopic observations of PSR B0540-69.3 were performed on 2002 January 9 with the *FOcal Reducer/low dispersion Spectrograph* (FORS1) on the 8.2m UT3 (MELIPAL) of the ESO/VLT, using a slit width of $1''$ and

Table 2. Log of VLT observations of PSR B0540-69.3 on 2002 January 9.

No.	Time UT	Exposure s	Airmass	Seeing^a arcsec
1	01:59:32.0	1320	1.43	1.25
2	02:23:25.0	1320	1.42	1.30
3	02:52:38.0	1320	1.41	1.18
4	03:16:31.0	1320	1.41	1.12
5	03:42:32.0	1320	1.41	1.24
6	04:06:25.0	1320	1.43	1.09
7	04:32:42.0	1320	1.45	0.88
LTT 3864	08:51:03.0	20	1.03	0.67

[a] Full width at half maximum of the stellar profile.

the grism GRIS_600B[1]. This grism has a dispersion of 50 Å/mm, or 1.18 Å/pixel, and a wavelength range of 3605–6060 Å. The optical path also includes a Linear Atmospheric Dispersion Corrector that compensates for the effects of atmospheric dispersion (Avila et al. 1997). The pixel scale of the detector is $0\rlap{.}{''}2$ per pixel. We obtained 7 exposures of 1320 s each (see Table 2), in total 154 minutes of exposure time. The position angle, PA=88°, was the same in all these exposures. The slit crosses the pulsar and its PWN as shown in Fig. 1. The mean seeing was ~ $1\rlap{.}{''}15$.
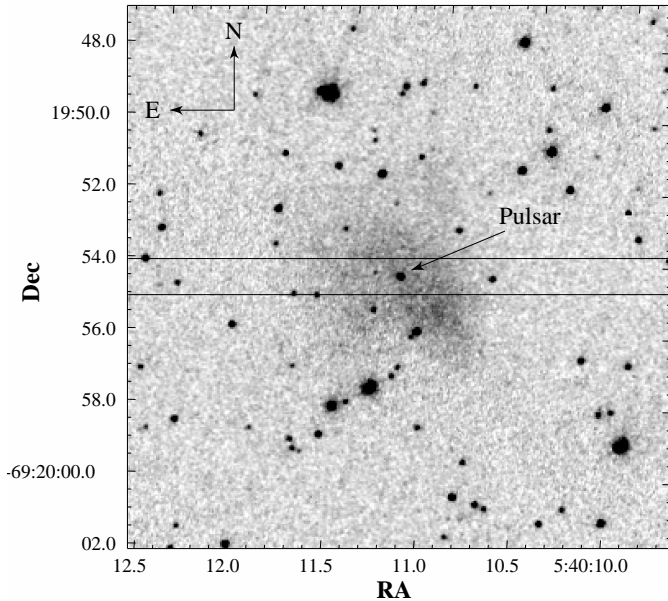

Fig. 1. A $15'' \times 15''$ image of the field around PSR B0540-69.3 obtained in the F547M band with the HST/WFPC2 (Morse 2003). The pulsar was exposed on the PC chip and its position is marked by an arrow. The slit position of the VLT observations is marked by thin parallel lines. The slit width is $1''$. The diffuse emission surrounding the pulsar is the pulsar wind nebula (PWN). Note its elongation in the NE-SW direction.

The spectroscopic images were bias-subtracted and flat-fielded using standard procedures within the NOAO IRAF Longslit package. We used the averaged sigma clipping algorithm avsigclip with the scale parameter set equal to none to combine the images. Wavelength calibration of the combined images was done using arc frames obtained with a helium-argon lamp. The spectra of the objects were then extracted from the 2D image using the apall and background tasks. Flux calibration of the spectra was accomplished by comparison with the spectrophotometric standard star LTT 3864 (Hamuy et al. 1994) observed on the same night (see Table 2). Atmospheric extinction corrections were performed using a spectroscopic
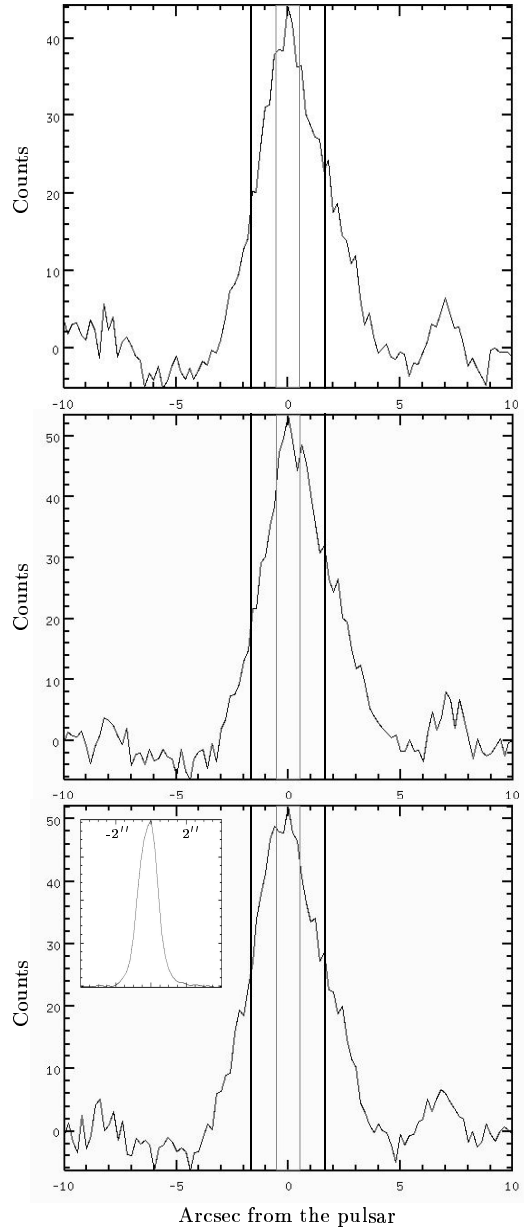

Fig. 2. Spatial profiles of PSR B0540-69.3 and its PWN along the slit in Fig. 1 (in counts, VLT data) at the continuum wavelengths 4600.0 Å, 5248.7 Å and 5450.0 Å, from top to bottom, respectively. In each panel the pulsar is assumed to sit at the main peak of the profile. Thin lines mark the six-pixel wide extraction window chosen for the spectral analysis of the pulsar (where 1 pixel corresponds to $0\rlap{.}{''}2$). The regions outside the thin lines, but within the solid lines have also a width of six pixels, and mark the regions used for the nebular subtraction in the spectral analysis. The spatial profile of a background star is shown in the inset in the bottom panel for comparison.

extinction table provided by ESO[2]. A significant flux (response) degradation was found at wavelengths below 3860 Å where the standard star spectrum displays many

---

[1] http://www.eso.org/instruments/fors1/grisms.html

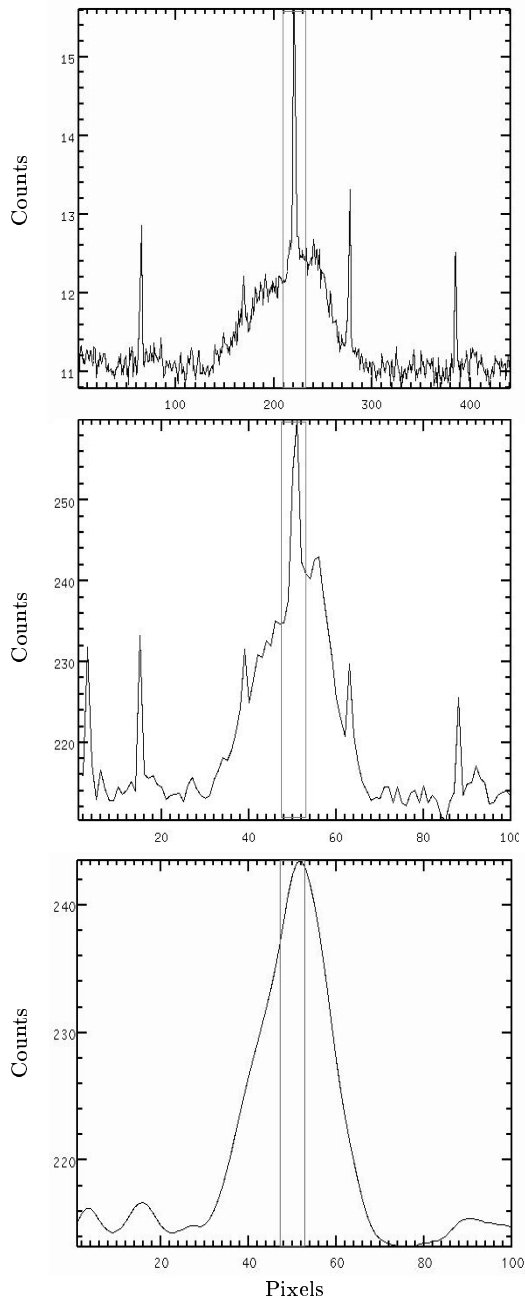[2] http://www.eso.org/observing/dfo/quality/UVES/files/ /atmoexan.tfits

Fig. 3. Spatial profiles as in Fig. 2, but using the HST/WFPC2/F547M image shown in Fig. 1. The pivot wavelength is 5483 Å. We show profiles obtained along the VLT slit with the spatial resolution of $0\farcs046$ provided by the PC chip pixel-size *(top)*, rebinned to the VLT CCD-pixel scale of $0\farcs2$ *(middle)*, and smoothed using a Gaussian with the FWHM of $1\farcs2$, comparable to the seeing value of the VLT observations, and then rebinned to the VLT CCD-pixel scale *(bottom)*. The VLT six pixel extraction window is marked by vertical lines.

deep spectral features, as well as in the very red end at $\lambda \gtrsim 6030$ Å. We therefore excluded these wavelength regions from our analysis.

2.2. Spectroscopy of the pulsar

As seen from Fig. 1 the pulsar is in the center of a bright compact nebula, which contaminates the flux from the pulsar. This contamination is particularly strong in nebular lines from the supernova remnant, but is also significant at continuum wavelengths where the spectrum of the extended object is expected to be dominated by synchrotron emission from the PWN.

In Fig. 2 we have plotted spatial profiles for the emission from the pulsar+nebula along the slit at several wavelengths where the contribution of nebular lines is negligible. Despite some minor variation of the shape of the profile with wavelength, the profile has a strong peak around the pulsar position. However, with a seeing of $\sim 1''$ the pulsar and nebular emissions are strongly blended. This is partially confirmed by a comparison of the profile with the PSF of a background star shown in the inset of the bottom panel of Fig. 2. To illustrate this further we have compared the VLT profiles with the profiles obtained from the HST/WFPC2/F547M image, shown in Fig. 1. From the F547M image we first extracted the data covered by the VLT slit, and then we averaged the emission across the slit for each position along the slit. The peak position of the flux along the slit varies with the wavelength of the spectroscopic image by $\lesssim 1$ VLT pixel. To take this into account in our test we extended the slit width by one pixel. In the first test case we kept the high spatial resolution in the HST image ($0\farcs046$, Fig. 3 top), while in the second case we averaged over a coarser pixel scale ($0\farcs2$) to simulate the VLT pixel size (Fig. 3 middle). In a third experiment we smoothed the initial image using a Gaussian with a FWHM of $1\farcs2$ to model the VLT seeing conditions and we then rebinned it to the VLT CCD-pixel scale (Fig. 3 bottom).

The pivot wavelength of the F547M filter is ~ 5483 Å, which is close to 5450 Å, chosen for the profile shown at the bottom of Fig. 2. As seen from Fig. 3, the pulsar is clearly resolved from the extended PWN at the PC chip spatial resolution as a narrow central peak on a broad ($\sim 7''$ in size) asymmetric pedestal formed by the PWN. It is still resolved at the VLT CCD-pixel scale of $0\farcs2$, while it is not resolved after the $1\farcs2$ smoothing. i.e., close to the seeing conditions of the VLT observations. Although the pulsar should contribute significantly to the flux within the spatial strip of six VLT pixels centered on the main peak of the whole profile, it is obvious that the nebula will contaminate severely the spectral VLT observations.

With this in mind, we extracted a 1D spectrum averaged over 6 pixels, equal to $1\farcs2$, along the slit centered at the pulsar position, as shown by thin vertical lines in Figs. 2 and 3. To subtract the nebular contribution we extracted 1D spectra averaged over six adjacent pixels to the east and an equal number to the west of the central strip, as indicated by thick lines in Fig. 2. An averaged spectrum was constructed from the two adjacent spectra and subtracted from the spectrum for the central region. The resulting spectrum contains no significant emission from

nebular lines, except for [O III] λλ4959, 5007, which has a high spatial variability within the nebula. The resulting spectrum, with the [O III]-feature removed, is presented in Fig. 4. As can be seen from this figure, our spectroscopic data agree well with the result by Hill et al. (1997) at the lower boundary of their 1σ uncertainty range, but give about 2−4 times higher flux than the photometric data of Middleditch et al. (1987). This can partly be understood from our method of correcting for the PWN emission. We averaged this by using the emission $1''\!.2 - 2''\!.4$ away from the center of the spatial profile. One problem is that Fig. 2 shows that the center of the profile in the VLT data may not coincide exactly with the pulsar position. A second, and more serious problem, is that the seeing spreads out much of the weak pulsar emission from the central region whereas seeing makes the PWN emission peak toward the center regardless of whether there is a pulsar or not. This will most likely lead to erroneous background subtraction so that the VLT spectrum shown in Fig. 4 is contaminated with significant PWN emission. The agreement with Hill et al. (1997) indicates that also their analysis overestimated the pulsar emission.

2.3. HST observations

The pulsar field has been imaged with the HST/WFPC2 several times in various bands mainly to study SNR 0540-69.3. For additional analysis of the optical emission from PSR B0540-69.3 and its PWN we retrieved some of these images from the HST archive.

The data using the wide and medium band filters F336W[3], F547M, and F791W, obtained on 1999 October 17 with 600 s, 800 s, and 400 s total exposure times, respectively (Morse 2003), are particularly useful for the continuum emission analysis since these filters do not cover any bright emission lines from the LMC or the supernova remnant. We also retrieved data sets for the narrow band F658N and wide band F555W filters, both of which were obtained on 1995 October 19 with 4000 s, and 600 s exposures, respectively (Caraveo et al. 2000).

The pulsar and its PWN are clearly detected on the PC chip in all these images. This is illustrated in Figs. 1 and 3 which present the data for the F547M band. The F658N filter includes the 6576−6604 Å range, which means that contamination from high-velocity Hα emission from the supernova remnant at central wavelength ∼ 6578 Å (Serafimovich et al. 2004) can enter into the filter passband, as well as [N II] emission from the LMC. This can also be seen in Fig. 3b of Caraveo et al. (2000) where it is shown that a filament passes across the pulsar along the NW direction. Although the pulsar stands out rather clearly on the image, the uneven background introduces some uncertainty to the estimated pulsar flux. The background contamination is more severe in the F555W band as it captures the bright [O III] λλ4959, 5007 Å lines

[3] http://www.stsci.edu/instruments/wfpc2/
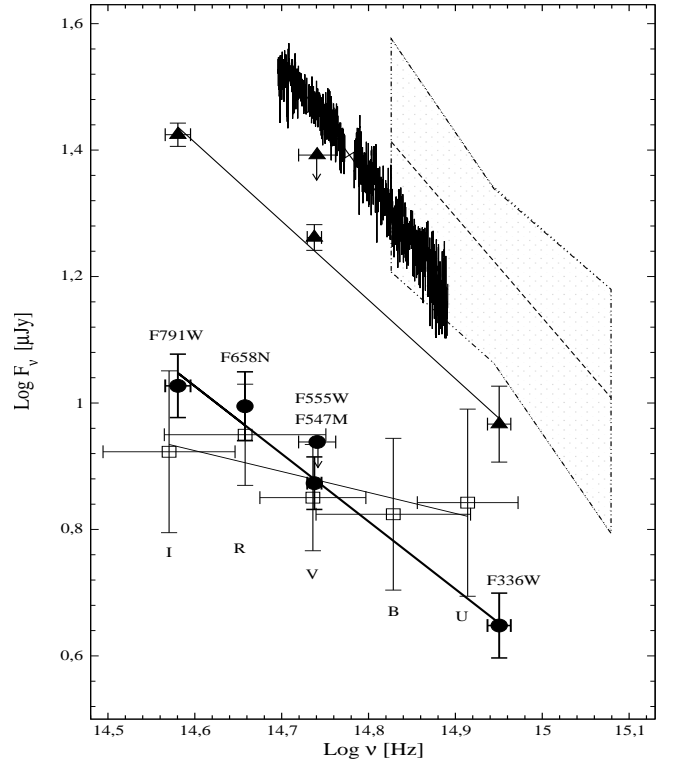/Wfpc2_hand_current/ch3_opticalfilters2.html#474439

Fig. 4. Optical spectrum of PSR B0540-69.3 obtained with different telescopes and instruments. The uppermost spectrum is the VLT spectrum for the 6-pixel area discussed in Figs. 2 and 3. The bright [O III] nebular lines have been removed. The dashed line and associated hexagonal region show the power law fit and 1σ-uncertainties of the UV spectrum obtained by Hill et al. (1997). Filled triangles show the HST photometry with a 10-pixel circular aperture to compare with the above spectra. Filled ellipses show our HST photometry results presented in Table 3. Open rectangles are the photometric UBVRI data by Middleditch et al. (1987). All data are dereddened using $E(B-V) = 0.20$. Solid lines show power law fits to the photometric data sets. Parameters of the fits are presented in Table 5.

which are much more difficult to spatially disentangle from the pulsar. The uneven background is most clearly seen in the image obtained with the F502N narrow band filter centered at these lines and overlapping with the F555W band. Therefore, the pulsar and PWN continuum flux measurements in the F555W band can only be considered as upper limits.

2.4. Photometry of the pulsar

For the photometry of the pulsar in the F336W, F547M, F555W, F658N, and F791W bands we used the Daophot and Photcal IRAF packages. To measure the pulsar flux we used circular apertures whose radii were determined from maximizing the signal-to-noise ratio S/N of the detected pulsar, and hence minimizing the magnitude error Δm

in each filter. For a point-like source, Δm and S/N are defined in the standard way as

$$\Delta m = \frac{2.5}{\ln 10}\left(\frac{S}{N}\right)^{-1}, \tag{1}$$

$$\frac{S}{N} = \left[\frac{N_c}{G} + A\sigma_N^2(1 + \frac{A}{A_{sky}})\right]^{-1/2} N_c, \tag{2}$$

where N_c is the flux in counts for a given aperture, σ_N^2 is the standard deviation in counts per pixel, A is the number of pixels in the aperture, G is the gain, and A_{sky} is the number of pixels in the annulus used for background measurements. The optimal aperture radii were found to be 2.5, 3.0, 4.0, 2.5, and 3.5 pixels, providing S/N of 8, 10, 25, 7.5, and 8 in the F336W, F547M, F555W, F658N, and F791W bands, respectively. Aperture corrections for the magnitudes were derived with the mkapfile package using several relatively bright nearby field stars in the PC images.

Pipeline-provided zeropoints PHOTFLAM (flux densities in wavelength units) and pivot wavelengths PHOTPLAM (in Å) taken from the fits header of each image were used for the flux calibration (see handbook for WFPC2[4]). Fluxes in units of μJy at the pivot frequencies $\nu = 10^8 c/\text{PHOTPLAM}$ (in Hz) were derived from the aperture corrected source counts using the expression

$$F_\nu = 10^{21}\frac{N_c}{c\,t_{exp}}PHOTFLAM \times PHOTPLAM^2 \tag{3}$$

where c is the speed of light in cgs units, and t_{exp} is the exposure time in seconds. We also calculated dereddened fluxes by multiplying F_ν with the extinction correction factors $k_{ext} = 10^{0.4k_i}$, where k_i is the interstellar extinction magnitude for the "i-th" passband determined using the extinction color excess toward SNR 0540-69.3. In order to compare with Middleditch et al. (1987) we have used the same values for $E(B-V)$ and R, i.e., 0.20 and 3.1, respectively, for both data sets, but a more recent extinction curve (Cardelli et al. 1989). We will discuss the extinction in greater detail in Sect. 2.8.

The results of the pulsar photometry are presented in Table 3 and shown in Fig. 4. The measured fluxes are about a factor of $2-4$ lower than the spectroscopic results in Sect. 2.2, except for the F555W filter which includes contamination from [O III]. The fluxes in this filter are presented as upper limits (see above). On the other hand, the HST photometry is compatible with the results obtained by Middleditch et al. (1987), but the uncertainties are several times smaller. Considered separately, our spectral and photometric measurements of the pulsar flux are in good agreement with previous results. However, they do not erase the significant discrepancy between these results (see Fig. 4), which is much larger than the uncertainty of our photometric measurements. The only plausible explanation to the discrepancy is that both the VLT and HST

Table 3. Broad-band fluxes[a] from PSR B0540-69.3.

Band	Pivot frequency log ν [Hz]	Measured flux log F_ν [μJy]	Dereddened flux log F_ν [μJy]
F336W	14.950(13)	0.243(51)	0.648(51)
F547M	14.737(8)	0.625(42)	0.873(42)
F555W	14.741(21)	≤ 0.69	≤ 0.94
F658N	14.658(1)	0.793(54)	0.995(54)
F791W	14.581(15)	0.874(50)	1.027(50)

[a] Hereafter numbers in the parentheses are uncertainties of the respective values. For example, 14.950(13) means 14.950 ± 0.013.

Table 4. Broad-band fluxes from a 10 pixel aperture around PSR B0540-69.3.

Band	Pivot frequence log ν [Hz]	Measured flux log F_ν [μJy]	Dereddened flux log F_ν [μJy]
F336W	14.950(13)	0.562(60)	0.967(60)
F547M	14.737(8)	1.013(20)	1.262(20)
F555W	14.741(21)	≤ 1.141	≤ 1.392
F791W	14.581(15)	1.271(18)	1.424(18)

Table 5. Parameters of the power law spectral fits ($F_\nu = F_{\nu_0}(\nu/\nu_0)^{-\alpha_\nu}$) of the pulsar data shown in Fig. 4.

Observations	α_ν	Log F_{ν_0}, $\nu_0=5.47 \times 10^{14}$ Hz [μJy]
VLT spectrum (this work)	1.88±0.01	1.469(2)
HST/FOS spectrum[a] (Hill et al. 1997)	1.6±0.4	1.228(115)
HST photometry (this work)	$1.07^{+0.20}_{-0.19}$	0.879(25)
10 pixel measurements (this work)	$1.24^{+0.19}_{-0.18}$	1.241(22)
Time-resolved photometry (Middleditch et al. 1987)	$0.26^{+0.45}_{-0.43}$	0.880(54)

[a] Log F_{ν_0} from Hill et al. (1997).

spectroscopy are strongly contaminated by the PWN, as already suggested in Sect. 2.2. As an additional test we measured the pulsar flux in the F336W, F547M, F555W, and F791W bands, using a circular aperture with a radius of 10 PC-pixels (corresponding to a total diameter of 0″92) centered on the pulsar, without subtraction of the background. These conditions should approximately reproduce the parameters of the spectral measurements within a circular aperture of almost the same diameter (0″86) made with the HST/FOS by Hill et al. (1997). The measured fluxes are presented in Table 4 and shown by triangles in Fig. 4. They are much closer to the HST and VLT spectral fluxes. The ~20%–70% discrepancy between these HST/WFPC2 and FOS fluxes must be considered as small compared with the large uncertainties of the FOS flux. Using a WFPC2 image Hill et al. (1997) estimated

the PWN contribution to be 30% in their FOS aperture. Note that this has not been accounted for in the spectrum in Fig. 4. However, their estimate assumed a uniform nebular background and was performed on an image with a PSF affected by spherical abberation. We have redone the exercise with the F574M image from 1999, and estimate that within a 10 pixel radius, the PWN contributes at least 50%. This can also be seen by comparing our accurate pulsar photometry with our 10 pixel test. The contamination of the HST/FOS spectrum would be even larger if the centering was not perfect. Although formal uncertainties of the VLT spectral flux appear to be smaller, the contamination from the nebula in the optical range is even stronger than in the UV, exceeding 250% at the redmost wavelengths of the VLT spectral range. This is natural, since the brightness of the PWN increases more steeply with the wavelength than does the pulsar brightness (see below).
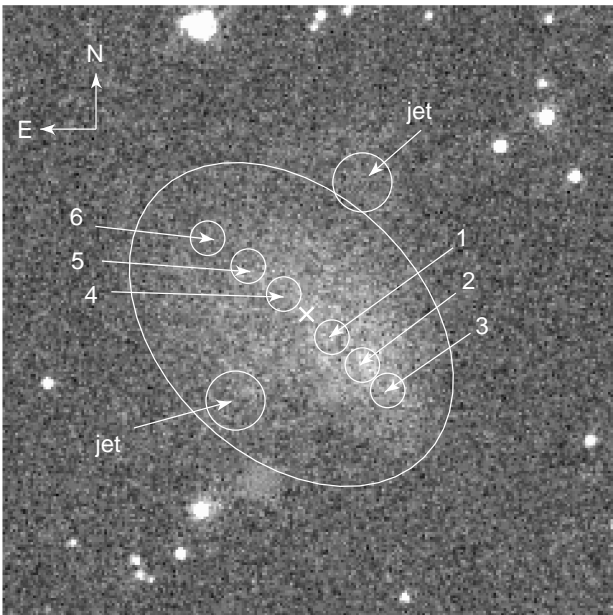

Fig. 5. $10'' \times 10''$ region of the field around PSR B0540-69.3 as observed in the F547M band with the HST/WFPC2 (Morse 2003). Background stars and the pulsar projected on the PWN have been subtracted off (cf. Fig. 1). We have marked six selected areas in the plane of the assumed torus as well as two areas in the jets. The ellipse shows the aperture used to measure the flux from the whole PWN. The pulsar position is marked by a white cross.

To summarize this part, we conclude that the current spectral data on the pulsar emission cannot be considered as reliable. Hopefully, narrow-slit spectroscopy with the HST/STIS could help to solve the contamination problem. Time resolved photometry with a high signal-to-noise is also a powerful tool to obtain the pulsed emission in a contaminated area, as can be seen even for the Crab pul-

sar (Sollerman 2003). On the other hand, our broadband HST spectrum of the pulsar, where the background from the nebula has been accurately subtracted off, can be considered as a fair estimate of the pulsar spectral energy distribution. As seen from Fig. 4, it is significantly steeper than found by Middleditch et al. (1987). If we define the spectrum as $F_\nu = F_{\nu_0} (\nu/\nu_0)^{-\alpha_\nu}$, then our power-law index is $\alpha_\nu = 1.07^{+0.20}_{-0.19}$ while that of Middleditch et al. is $\alpha_\nu = 0.33 \pm 0.45$ (see Table 5) using updated dereddening corrections. (The method how to calculate these power-law indices is described in Sect. 2.5.) The flatter spectrum of Middleditch et al. is partially due to a spectral jump upwards for the U band, whereas our flux toward the overlapping F336W band goes down smoothly, as would be expected from the extrapolation of the longer wavelength data. This upturn in Middleditch et al. (1987) could be due to a systematic error in their U band flux. We note that also the Crab-pulsar broadband spectrum by Middleditch et al. (1987) has a significant excess in the U band, which has not been confirmed by more recent spectral observations extending even further into the UV (Sollerman et al. 2000). However, possible variability of the pulsar emission in the UV range cannot be excluded as another cause of the difference between our results for PSR B0540-69.3 and the result by Middleditch et al. (1987). We also note that while we are studying the time-integrated flux, Middleditch et al. studied the time-resolved flux, albeit with a poor signal-to-noise and spatial resolution.

2.5. Photometry of the PWN

Using the HST images discussed in Sect. 2.3 we have also made aperture photometry of the continuum emission from the whole PWN, as well as different parts of it selected on the basis of the morphology of the nebula. For this analysis we have discarded the F555W and F658N filters due to the risk of contamination by the [O III] and Hα emission from the SNR. To make an accurate analysis we first subtracted off all stars in the immediate vicinity of the nebula as well as stars which overlap with the PWN. We also subtracted off the pulsar. For the subtraction we used the allstar task within the Daophot package (Stetson 1987) and for a comparison also the credit task within the Crutil package. There was no significant difference in the subtraction results using the two methods. The photometry was performed with the Isophote package (Jedrzejewski 1987).

The PWN of PSR B0540-69.3 has a remarkable structure that can be seen clearly in Figs. 1 and 5. To sample different regions, we have put circle apertures at eight different positions, one in each jet (with an aperture radius of 12 pixels, i.e. $0''\!.55$), and three (with an aperture radius of 7 pixels, i.e. $0''\!.32$) on each side of the pulsar in the plane of the presumed torus. We also constructed an elliptical aperture with a 74 pixel (i.e. $3''\!.4$) semi-major axis, ellipticity 0.3, and positional angle 45 degrees, that encapsulates the entire PWN (cf. Fig. 5), except for the weak northern
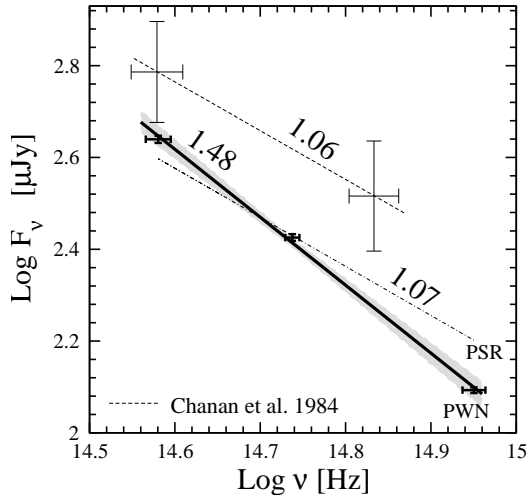
Fig. 6. Broad-band fluxes from the full PWN obtained with the HST (thick errorbars) using the elliptical aperture shown in Fig. 5. The thick line and filled area provide the best power-law fit to the data and its 1σ uncertainties, respectively (see Table 6). Previous data by Chanan et al. (1984) in the I and B bands (thin errorbars and dashed line), as well as the slope of the pulsar spectrum (cf. Fig. 4), normalized arbitrary (dot-dashed line), are shown for comparison. Numbers near the lines denote spectral indices. Note that Chanan et al. (1984) did not correct for contaminating flux from background stars and nebular line emission.

jet. The apertures are marked and identified in Fig. 5. All regions show emission in all filters, except for the northern jet ("North Jet") and "Area 6" which are not detected in the F336W band. For these two regions we provide 3σ upper limits, based on the standard sky deviations per pixel within the respective areas. The results are presented in Table 6.

As expected, the measured broadband spectra from the whole PWN and its different parts are well described by power-laws with negative spectral index, which confirm the nonthermal origin of the continuum nebular emission. To derive the spectral indices we used the following method. For each data point we made Gaussian fits in log space to the flux and the filter function. We then simulated 10,000 sets of data using a Monte Carlo code which uses a fast portable random generator[5], and for each data set we made a linear fit to obtain a power-law. The power laws were then ordered in increasing value of the power law index, and the median value was chosen to represent the best fit power law. In order not to be dependent on the seed value for the random number series, we ran the code 500 times with different seed values, and then took the average value for the power-law index to be the final estimate of the index. The filled hexagons in Figs. 6 and 7 show 1σ errors estimated from the constraint that 68% of the constructed power laws must lie within a 1σ area.

The advantage of using a Monte Carlo code rather than simple weighted means to estimate power law indices is that we can allow and test for non-Gaussian distributions in log space. This is obviously not the case with a steep spectrum, non-Gaussian filter functions, as well as upper limits. Our tests, however, show that the filters are narrow enough to get good fits from Gaussian fits to the points with estimated fluxes. From our Monte Carlo code approach it is also easy to estimate the error of the derived power-law index. The same approach was also used to fit the pulsar spectrum in Sect. 2.4. The results are presented in Tables 5, 6 and shown for the emission from the whole PWN in Fig. 6 and from its different regions in Fig. 7.

According to Chanan et al. (1984) the fluxes (in μJy) from the whole PWN are log $F_B \approx 2.19$ and log$F_I \approx 2.63$. Our values are much lower ($\sim 60\%$ and $\sim 40\%$, respectively, see Fig. 6). The main reason is that we have subtracted off the pulsar and stars overlapping with the PWN, whereas these objects are not resolved from the PWN in the B and I images of Chanan et al. (1984) which were obtained at $1\farcs2$-$1\farcs4$ seeing. Hence, their B and I fluxes are contaminated by non-PWN emission and this changes significantly the derived spectral slope of the PWN: Chanan et al. (1984) obtain $\alpha_\nu = 1.06$ (after dereddening with $E(B - V) = 0.20$) whereas we get $\alpha_\nu = 1.48^{+0.09}_{-0.08}$ from the HST data.

Compared with the pulsar the whole PWN is more than an order of magnitude brighter, and its spectrum is significantly softer (cf. Tables 3 and 6 and thick solid and thin dot-dashed lines in Fig. 6). This shows that the NS spindown power is transformed to optical emission more efficiently in the PWN than in the pulsar magnetosphere (see below).

A more detailed study shows that the spectrum may vary over the PWN. This is seen from Fig. 7 where we have plotted the results of the HST photometry of different parts of the PWN and the respective power-law spectral fits (thick lines) with their 1σ uncertainties (uniformly filled regions). Stripe-filled regions show extensions of the fits in cases when only upper limits in one of the three bands were obtained. The spectral hardness of some parts of the nebula is comparable or even higher to that of the pulsar, as it is for "Areas 1, 5, 6", and both "jets". The spectra of the N-E part of the torus-like structure appear to become harder toward the outer boundary of the nebula. On the other hand, "Area 2", which is the brightest among the three selected areas S-W of the pulsar, has a steeper spectrum than its closest neighbors.

Another feature of the spatial flux and spectral variations of the PWN is demonstrated by Figs. 8 and 9 where we have plotted the distributions of the frequency-integrated optical fluxes F, derived from the above spectral fits, and the spectral indices α_ν versus the angular distance from the pulsar along the major axis of the torus-like structure of the PWN. There is a significant decrease of the surface brightness going from the brightest area, area 2, toward the N-E edge of the torus (Fig. 8). The brightness difference exceeds the 6-sigma level of the un-

Table 6. Broad-band fluxes and power-law fit ($F_\nu = F_{\nu_0}(\nu/\nu_0)^{-\alpha_\nu}$) parameters of the emission from different regions of the PWN marked in Fig. 5. Their offsets from the pulsar and areas are given in the 2nd column. Upper and lower values for each entry of the fluxes are the measured and dereddened fluxes with $E(B-V) = 0.20$ ($A_V = 0.62$), respectively.

Region	Offset	Area arcsec^2	F336W	F547M Log flux from the area	F791W μJy	α_ν	$\log F_{\nu_0}$, $\nu_0 = 5.47 \times 10^{14}$ Hz μJy
Full PWN	0.″000 N	10.92	1.688(6)	2.177(7)	2.482(8)	−	−
	0.″000 W		2.093(6)	2.426(7)	2.640(8)	$1.48^{+(9)}_{-(8)}$	2.414(12)
Area 1	0.″455 S	0.33	0.350(116)	0.647(94)	0.991(48)	−	−
	0.″409 W		0.755(116)	0.896(94)	1.144(48)	$1.09^{+(33)}_{-(30)}$	0.949(50)
Area 2	1.″001 S	0.33	0.224(146)	0.766(35)	1.054(30)	−	−
	0.″910 W		0.629(146)	1.015(35)	1.207(48)	$1.58^{+(43)}_{-(42)}$	0.980(45)
Area 3	1.″456 S	0.33	0.176(147)	0.628(60)	0.892(45)	−	−
	1.″365 W		0.581(147)	0.877(60)	1.045(45)	$1.28^{+(43)}_{-(41)}$	0.856(49)
Area 4	0.″409 N	0.33	0.114(236)	0.582(128)	0.868(102)	−	−
	0.″364 E		0.519(236)	0.831(128)	1.021(102)	$1.49^{+(67)}_{-(59)}$	0.806(58)
Area 5	1.″046 N	0.33	0.252(140)	0.485(106)	0.791(64)	−	−
	0.″865 E		0.657(140)	0.734(128)	0.944(64)	$0.92^{+(37)}_{-(33)}$	0.786(58)
Area 6	1.″775 N	0.33	$\le 0.032^a$	0.239(98)	0.377(102)	−	−
	1.″365 E		≤ 0.437	0.488(98)	0.530(102)	$0.27^{+(91)}_{-(90)}$	0.488(98)
North Jet	1.″001 N	0.96	$\le 0.265^a$	0.642(50)	0.875(68)	−	−
	2.″366 W		≤ 0.670	0.891(50)	1.028(68)	$0.87^{+(56)}_{-(54)}$	0.891(51)
South Jet	1.″274 S	0.96	0.483(128)	0.796(43)	1.105(33)	−	−
	1.″547 W		0.888(128)	1.045(43)	1.258(33)	$1.03^{+(35)}_{-(30)}$	1.077(38)

^{a} 3σ upper limit.

certainty level of the dimmest area, area 6, and shows an asymmetry of the flux distribution with respect to the pulsar position which is similar to what is also seen in X-rays with Chandra/HRC[6]. In the Crab PWN, the brightness difference between the near and far sides of the torus, for a given viewing angle, is usually explained by Doppler boosting and relativistic aberration of the synchrotron radiation from relativistic particles flowing at subrelativistic velocities from the pulsar in the torus plane, assuming an axisymmetric distribution of the pulsar wind around the pulsar rotation axis (e.g., Komissarov & Lubarsky 2004). However, the considerable asymmetry of the brightness distribution between the two sides (N-E versus S-W) of the torus of PSR B0540-69.3, as seen in projection, makes axial symmetry less obvious in a general picture. This is further strengthened by a similar asymmetry in the torus-plane, albeit less pronounced, seen in recent X-ray images of the Crab PWN (e.g., Mori et al 2004). The asymmetry

can be produced either by breakdown of axial symmetry in the pulsar wind (e.g., due to plasma instabilities) or by inhomogeneity of the PWN environment, i.e., an asymmetry of the SN ejecta. The latter is indeed indicated by the asymmetric distribution of optical filaments projected on the PWN of PSR B0540-69.3 (Morse 2003), as well as the general redshift of the gas emitting optical lines (Kirshner et al. 1989; Serafimovich et al. 2004).

The spatial distributions of F and α_ν in Figs. 8 and 9 appear to have similar shapes and may suggest a harder spectrum from the dimmer outer areas of the PWN. The data are, however, rather uncertain and a constant spectral index of ~ 1 seems to be compatible with all errorbars in Fig. 9. To check that more thoroughly we analyzed the α_ν–F distribution presented in Fig. 10 which also includes both jet areas. A linear regression fit to α_ν versus $\log(F)$ using the method described in this Sect. above yields

[6] chandra.harvard.edu/photo/2004/snr0540

$$\alpha_\nu = 19.44 + 1.35 \log(F) \qquad (4)$$
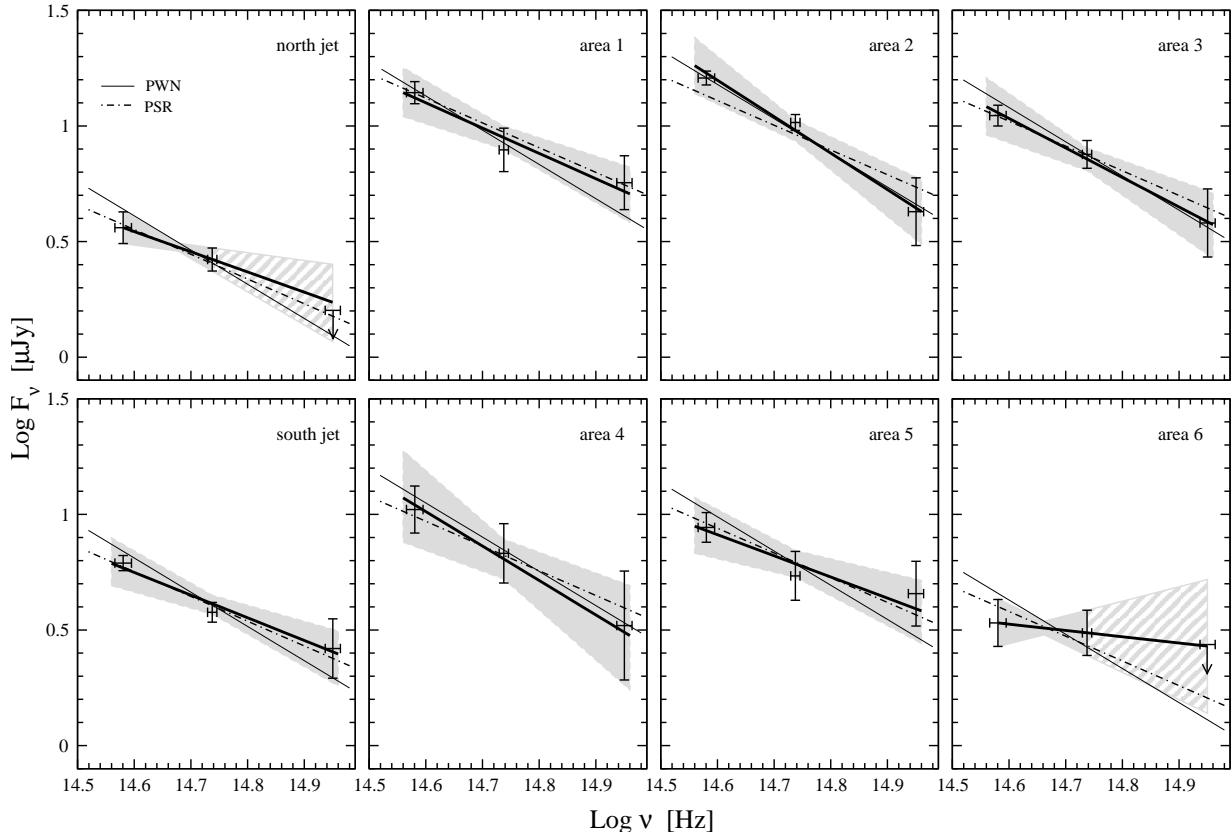
Fig. 7. Broad-band optical spectra for all the selected areas of the PWN shown in Fig. 5. The filled hexagons show 1σ uncertainty regions around the best-fit power laws indicated by thick lines. The fluxes of the "jets" are normalized to a 7-pixel aperture area for convenience in order to compare their brightnesses with the brightness of other parts of the PWN. The spectral slopes of the whole PWN (thin lines) and the pulsar (dot-dashed lines) are shown for comparison. The dot-dashed and thin lines have been shifted arbitrarily in the vertical direction.

This is shown by a solid line in Fig. 10, and indicates that brighter structures of the PWN have a steeper spectral index. The gray area shows the 1σ uncertainty of the fit. The range of the line slopes within this area is $1.35^{+1.02}_{-0.98}$. A zero slope, and thus no correlation, is allowed only if we increase the uncertainty area to 1.4σ. This value can be considered as an overall significance of a possible α_ν-$\log(F)$ correlation. We also checked the spectral index-flux correlation using the spectral fit parameter F_{ν_0} as well as the measured flux value F_ν in the F547M band (see Table 6) instead of the derived F and got only a slightly tighter correlation.

Therefore, deeper observations of the PWN are needed to probe a correlation between the brightness and the spectral index which is indeed only marginally indicated by the current optical data. A study of the index-flux distribution in X-rays would also be useful for the PWN of PSR B0540-69.3, as has recently been done for the Crab PWN (Mori et al. 2004). The study of Mori et al. shows that for brightnesses above ~ 0.7 counts s^{-1} arcsec^{-2} there is a hint that (cf. their Fig. 3) the spectral index of the torus region increases with the surface brightness, as marginally indicated also in our case for PSR B0540-69.3. However, including

brightnesses down to ~ 0.4 counts s^{-1} arcsec^{-2}, the spectral index – surface brightness distribution appears flat. The indices of the Crab jet are generally smaller compared to those of peripheral PWN regions although their surface brightnesses are comparable (Mori et al. 2004). In the case of PSR B0540-69.3 the correlation may be enhanced by a larger brightness asymmetry of the PWN. We note that such a correlation, as well as a flat index versus flux distribution, contradicts simple expectations from synchrotron cooling of relativistic particles which suggest a softening of the underlying electron spectrum toward the PWN boundary. In this picture, the fainter outer regions of the nebula would emit softer spectra. However, this simple picture does not work even for the much better studied Crab, where the PWN torus does not change its size significantly from radio to hard X-rays, whereas the respective cooling times differ by many orders of a magnitude implying much larger extents in the radio and optical than in X-rays. The same appears to be true for PSR B0540-69.3 (Caraveo et al. 2000). This is not yet explained, neither by the classical isotropic pulsar-wind model of a PWN by Kennel & Coroniti (1984), nor by modern MHD versions of it (Bogovalov & Khangoulyan 2002;
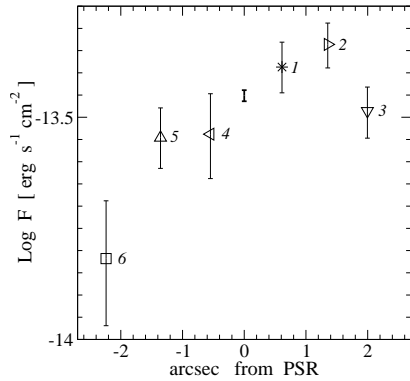
Fig. 8. Optical fluxes F in the $(3.8 - 8.9) \times 10^{14}$ Hz frequency range from different parts of the PWN marked according to notations in Fig. 5 *versus* the distance from the pulsar along the major axis of the torus-like structure of the PWN. Negative and positive labels on the horizontal axis correspond to the N-E and S-W directions from the pulsar, respectively. The bold errorbar at the center shows the flux from the whole PWN rescaled to the 7 pixel aperture area used for measurements in "Areas 1 – 6".
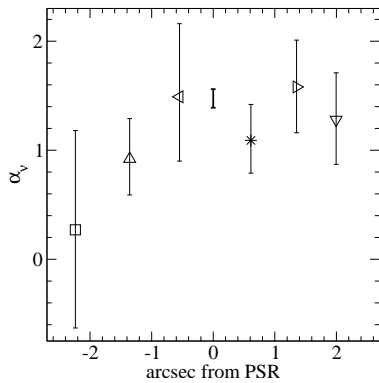

Fig. 9. Same as in Fig. 8 but for spectral indices. Symbols denote the same area numbers as in Fig. 8.

Komissarov & Lubarsky 2004;   Del Zanna et al. 2004) despite the fact that these also include anisotropy of the wind along the pulsar rotation axis, and can qualitatively explain the observed torus-jet structure invoking a complicated axisymmetric picture of the wind termination shock in the internal region of the PWN.

2.6. Proper motion and astrometry of PSR B0540-69.3.

The position of PSR B0540-69.3 is defined on the HST PC chip frames with an accuracy of better than 0.17 PC pixels which corresponds to $0\overset{''}{.}0077$. This is only a factor of ~ 1.5 larger than the yearly proper motion value reported by Manchester et al. (1993b), see Table 1. This allows a direct estimate of the proper motion of the pulsar using accurate superposition of the F555W and F547M images taken at epochs separated by 4 years (see Sect. 2.3). We used the
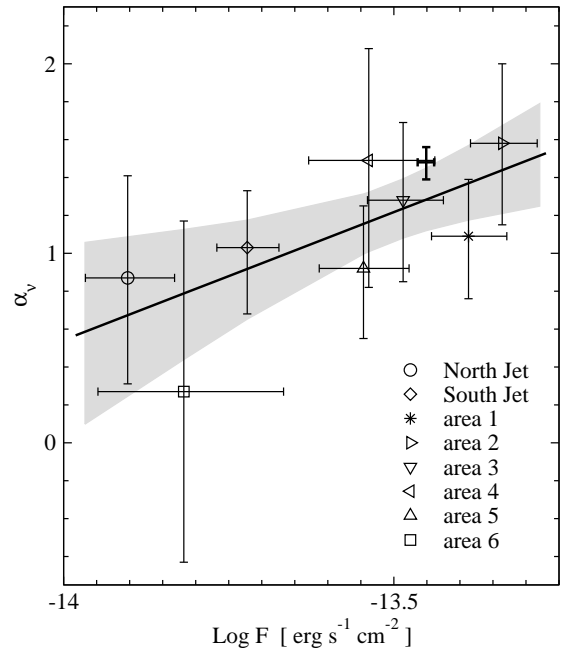

Fig. 10. Spectral index α_ν versus optical flux, $\log(F)$, in the $(3.8 - 8.9) \times 10^{14}$ Hz range for the different areas of the PWN marked according to Fig. 5. The thick solid line shows the best fit linear model given by Eq. (4). The point marked by bold errorbars shows the parameters for the full PWN rescaled to a 7-pixel aperture (cf. Fig. 8). The gray area shows the 1σ uncertainty area for possible linear fits to the data points using the method described in Sect. 2.5. A zero slope correlation is excluded at the 1.4σ level.

positions of 9 reference stars to construct the coordinate transformation between the two images with the IRAF routines geomap and gregister. The *rms* errors of the transformation fit were 0.078 and 4.6×10^{-4} of the PC pixel size in RA and DEC, respectively, with residuals being ≤ 0.156 pixels in RA and 8.1×10^{-4} pixels in DEC. Using imcentroid for measuring the coordinates of the pulsar we find a shift of 0.431 ± 0.203 pixels between its positions for a time difference of 3.995 years, where the error accounts for the centroid and transformation uncertainties. This corresponds to a proper motion $\mu = 4.9 \pm 2.3$ mas y^{-1} in the South-East direction at a position angle of $108\overset{\circ}{.}7 \pm 32\overset{\circ}{.}9$ (along the southern jet). The significance of this result is low and can be considered only as an attempt to make a first direct measurement of the proper motion. Based on the displacement between the pulsar optical position and the center of the PWN, as seen in radio, Manchester et al. (1993b) argued for a similar value of the proper motion but in the South-West direction (in the plane of the torus). We note that the proper motion of the Crab pulsar is aligned with the symmetry axis of the inner Crab nebula, as defined by the direction of the X-ray jet discovered by ROSAT (Caraveo et al. 1999), and that a similar situation applies to the Vela pulsar (De Luca et al. 2000; Caraveo et al. 2001; Dodson et al. 2003). If our estimates are close to reality, we have the intriguing situation that

Table 7. Coordinates of PSR B0540-69.3.

Range	R.A.(J2000) $05^h 40^m\ +$	Dec. (J2000) $-69° 19'\ +$
X-ray[a]	$11^s.0 \pm 0^s.7$	$57''.4 \pm 2''.0$
Optical[b]	$10^s.99 \pm 0^s.18$	$55''.1 \pm 0''.5$
Radio[c]	$11^s.1$	$57''.5$
X-ray[d]	$11^s.221 \pm 0^s.132$	$54''.98 \pm 0''.7$
Optical[e]	$11^s.173 \pm 0^s.121$	$54''.41 \pm 0''.7$

[a] Seward et al. (1984); [b] Caraveo et al. (1992);
[c] Manchester et al. (1993a); [d] Kaaret et al. (2001);
[e] this work

all these three young pulsars appear to move along the jet axis. A difference is, however, that while the Crab and Vela pulsars both have transverse velocities of ~ 130 km s^{-1}, our results for PSR B0540-69.3 indicate a higher transverse velocity 1190 ± 560 km s^{-1}, assuming a distance to the LMC of 51 kpc (Panagia 2004). A third epoch of HST imaging to confirm the large value and direction for the transverse velocity is clearly needed to establish this result at a higher significance level. Based on our proper motion estimates a level of $\gtrsim 3\sigma$ can be achieved starting from the beginning of 2005.

We also determined the coordinates of the pulsar in the F547M image using seven GSC-II stars visible within the PC chip frame and the IRAF routines ccmap, cctran, and ccsetwcs. The formal rms errors of the astrometric fit are $0''.423$ and $0''.472$ in the RA and DEC, respectively. Combined with the nominal GSC-II catalog accuracy of $0''.5$, this gives an accuracy of the position of the pulsar of $0''.655$ and $0''.688$ in RA and DEC, respectively. In Table 7 we compare our astrometry with previous results. We note the good agreement between our measurement and the latest Chandra result (Kaaret et al. 2001).

2.7. X-ray spectrum

2.7.1. Interstellar absorption

The new optical results allow us to update the multiwavelength picture of the emission of PSR B0540-69.3. We will discuss this in greater detail in Sect. 3. Before establishing the overall spectrum, one first needs to accurately correct for absorption and scattering by the interstellar gas and dust. In a recent analysis of time-resolved Chandra data, Kaaret et al. (2001) argue that the pulsed emission of PSR B0540-69.3 can be approximated by a power-law $F_E = F_{E_0}(E/E_0)^{-\alpha_E}$ with $\alpha_E = 0.83 \pm 0.13$ within the photon energy range $E = 0.6 - 10.0$ keV range, provided that the foreground photoelectric absorption is caused by gas with Milky Way (MW) abundances and a column density of $N_{HI} = 4.6 \times 10^{21}$ cm^{-2}. A similar number ($N_{HI} = 4.0^{+0.6}_{-0.4} \times 10^{21}$ cm^{-2}) was estimated by Finley et al. (1993) analyzing ROSAT X-ray data.

However, the use of MW abundances is obviously a simplification for PSR B0540-69.3. As a matter of fact, only a fraction of the photoelectric absorption is likely to occur in the Milky Way. The recent Parkes 21 cm multibeam survey of the LMC (Staveley-Smith et al. 2003) shows that the MW contribution to the column density in the direction to PSR B0540-69.3 is just $N_{HI} \approx 0.6 \times 10^{21}$ cm^{-2}. This survey also shows that the maximum value of N_{HI} in the LMC is $\sim 5.6 \times 10^{21}$ cm^{-2}, and that this occurs close to the position of PSR B0540-69.3. This is consistent with the hydrogen column density found by fitting the wings of the Lyα absorption profile for the neighboring LMC star Sk -69 265, $N_{HI} = (5 \pm 0.5) \times 10^{21}$ cm^{-2} (Gordon et al. 2003). It is quite likely that PSR B0540-69.3 could have a similarly high column density, especially since its dispersion measure (see Table 1) is $\sim 50\%$ higher than for any other pulsar in the LMC (Crawford et al. 2001). A rough estimate of the LMC part of N_{HI} for PSR B0540-69.3 can be obtained from scaling of the estimated column density for SNR 1987A and its neighboring star, "Star 2". Michael et al. (2002) used LMC abundances to derive $N_{HI}(\text{LMC}) = 2.5^{+0.4}_{-0.3} \times 10^{21}$ cm^{-2} for SNR 1987A, and Scuderi et al. (1996) obtained $N_{HI}(\text{LMC}) = 3.4^{+1.0}_{-0.9} \times 10^{21}$ cm^{-2} for Star 2 allowing for a foreground MW contribution of 0.6×10^{21} cm^{-2}. We adopt $N_{HI}(\text{LMC}) = 2.9^{+1.0}_{-0.9} \times 10^{21}$ cm^{-2} for SNR 1987A and Star 2. Assuming that SNR 1987A and PSR B0540-69.3 suffer similar amounts of LMC absorption in proportion to the LMC 21 cm emission (Staveley-Smith et al. 2003) along their respective lines of sight, we obtain $N_{HI}^{0540} \approx N_{HI}^{87A}$ HI^{0540}/HI$^{87A} \approx 5.5^{+1.9}_{-1.7} \times 10^{21}$ cm^{-2}, where HI$^{0540} = 32.00$ Jy/beam and HI$^{87A} = 16.75$ Jy/beam are the line flux densities toward the pulsar and SNR 1987A, respectively, according to the Parkes survey data base[7]. The assumptions used to obtain this result for N_{HI}^{0540} are of course uncertain, but the result points in the same direction as the estimates from the 21 cm emission, Sk -69 265 and the pulsar dispersion measure discussed above, i.e., the column density for PSR B0540-69.3 is high. Assuming that the 21 cm emission at the position of PSR B0540-69.3 marks an upper limit to its $N_{HI}(\text{LMC})$, we can limit the range to $N_{HI}^{0540} = (4.6 \pm 1.0) \times 10^{21}$ cm^{-2}. This is similar to what was used by Kaaret et al. (2001), but with the important difference that the X-ray absorption is not mainly Galactic, but arises in the LMC.

To illustrate the effect of LMC abundances we show in Fig. 11 the ratio of photoelectric cross sections (per hydrogen atom) in the LMC and MW for the energy range 0.1–10 keV. We will refer to this ratio as $f(E)$. The drop in $f(E)$ at $E > 0.28$ keV (the K-shell edge of carbon) just reflects the lower metal content in the LMC compared to the Galaxy. For the MW we have used the abundances in Morrison & McCammon (1983, henceforth MM83), and for LMC we have adopted the abundances of He, C, N, O, Mg, Si and Fe from Korn et al. (2002). We have also included the elements Ne, Na, Al, S, Ar and Ca for which we have assumed that the LMC abundances are 0.4, 0.4, 0.5, 0.4, 0.5 and 0.5 times the solar values in MM83, respectively. The exact numbers for these elements are not

---

[7] www.atnf.csiro.au/research/multibeam/release/

important for our analysis since the absorption is dominated by C, N, O and Fe in the energy range we are most interested in. We assume that the interstellar gas is neutral, and we disregard dust. Photoionization cross sections were taken from the code used in Lundqvist & Fransson (1996) with further updates for Na, Mg, Al, Ar, & Ca using the TOPbase archive (Cunto & Mendoza 1993), as well as for He (Samson et al 1994; Pont & Shakeshaft 1995). We have tested this code against the results of MM83 for solar abundances, and the cross sections agree to the same level of accuracy as the recent cross sections compiled by Wilms et al. (2000). The comparison against MM83 is relevant as Kaaret et al. (2001) did their analysis using XSPEC Ver. 10.0 which uses data fully compatible with MM83. Figure 11 shows that LMC abundances strongly suppress the photoelectric absorption, and that C and O are particularly important constituents at the energies for which Kaaret et al. (2001) claim photoelectric absorption is most important for the observed pulsar spectrum, i.e., at $\lesssim 1$ keV.
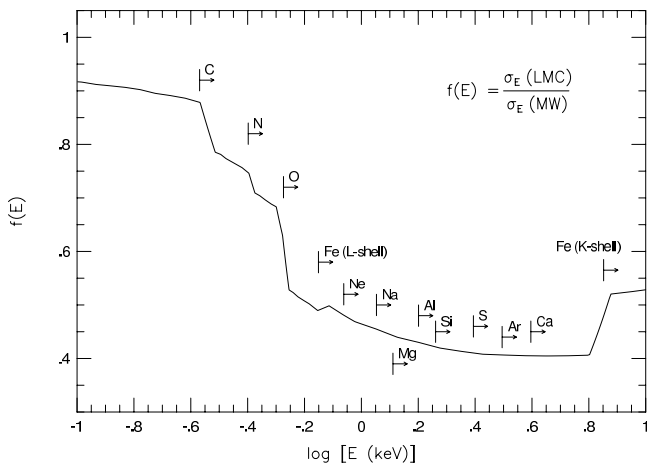

Fig. 11. Ratio of photoelectric absorption per hydrogen atom in the LMC and Milky Way for the energy range 0.1–10 keV. Arrows mark at which energy each element starts to contribute to the photoelectric absorption. The absorbing gas is assumed to be neutral. The gradual changes of $f(E)$ across absorption edges are due to moderate zoning of the photon energy in the code used for the cross section calculations. See text for further details.

We have used the function $f(E)$ in combination with the results of MM83 to see how LMC abundances may affect conclusions about the derived spectrum of PSR B0540-69.3. If we assume that the pulsar emits a pulsed power-law spectrum with slope $\alpha_E = -0.83$ in the range $0.6 - 10.0$ keV, as argued for by Kaaret et al. (2001) and marked in Fig. 12 as a straight dotted line, the attenuated spectrum should look like the solid line in Fig. 12 after passage through a column density of neutral hydrogen in the Milky Way with a value of $N_{HI}(MW) = 4.6 \times 10^{21}$ cm^{-2}. If we disregard possible effects of an accurate treat-

ment for the response matrix of Chandra, we can deabsorb this spectrum with a more likely composition for the photoelectrically absorbing gas. For this we have chosen $N_{HI}(MW) = 0.6 \times 10^{21}$ cm^{-2} and $N_{HI}(LMC) = 5.0 \times 10^{21}$ cm^{-2}. The deabsorbed spectrum is marked by the upper dashed line in Fig. 12. At the lower energy limit of the fit by Kaaret et al. (2001), i.e., at 0.6 keV, the deabsorbed spectrum undershoots by a factor of ~ 2.9 compared to the power-law, but on the other hand overshoots by orders of magnitude at energies below the K-shell edge of carbon. The latter can be fixed by just lowering $N_{HI}(LMC)$ to $\lesssim 4.3 \times 10^{21}$ cm^{-2}, i.e., still consistent with the likely range argued for earlier in this section. The spectrum would in that case undershoot by a factor of $\gtrsim 3.8$ at 0.6 keV compared to the power-law. The assumption of a power-law spectrum at energies below a few keV, where the photoelectric absorption sets in, is of course uncertain. Our results could indicate that the intrinsic spectrum is not a power-law, but actually falls below the power-law at 0.6 keV. However, before jumping to such a conclusion we need to check another possible source of X-ray absorption, namely the supernova ejecta.
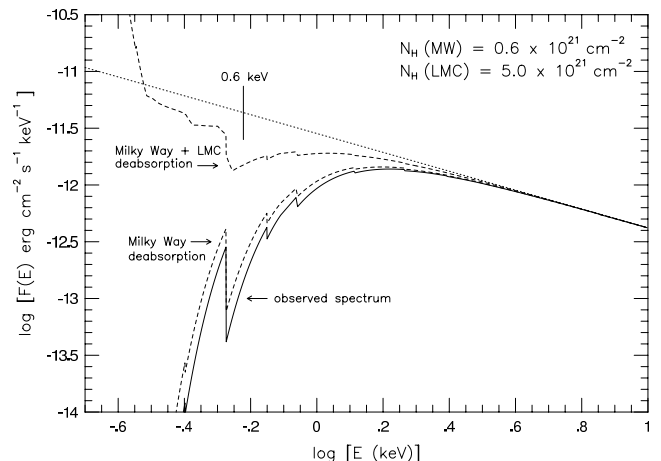

Fig. 12. Soft X-ray spectrum of the pulsed emission from PSR B0540-69.3. The dotted line shows the intrinsic power-law spectrum argued for by Kaaret et al. (2001), and the solid line shows the attenuated spectrum after passing through a column of gas with MW abundances, $N_{HI}(MW) = 4.6 \times 10^{21}$ cm^{-2}. The lower dashed line shows deabsorption using a more realistic value for the MW contribution, $N_{HI}(MW) = 0.6 \times 10^{21}$ cm^{-2}, and the upper dashed line shows further deabsorption with the value $N_{HI}(LMC) = 5.0 \times 10^{21}$ cm^{-2} for LMC, which is close to the maximum value found for the LMC as a whole according to Staveley-Smith et al. (2003). The vertical bar at 0.6 keV marks the energy above which Kaaret et al. (2001) fitted their power-law to the deabsorbed spectrum.
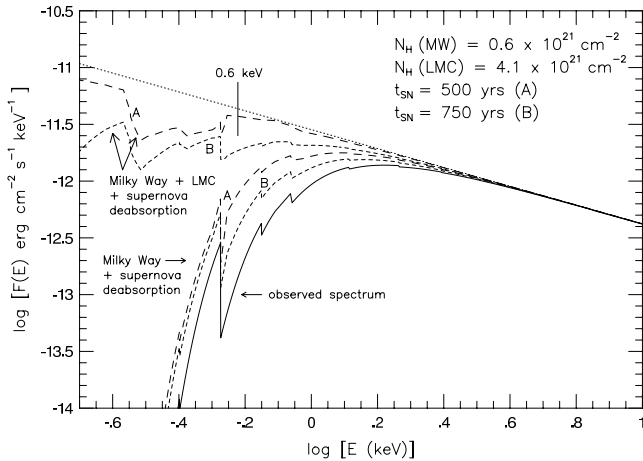
Fig. 13. Same as Fig. 12, but with a lower value for the LMC deabsorption, $N_{\mathrm{HI}}(\mathrm{LMC}) = 4.1 \times 10^{21}$ cm^{-2}. Deabsorption due to supernova ejecta has also been included, assuming the same structure as in SN 1987A. The structure of SN 1987A on day 118 (Blinnikov et al. 2000) was expanded homologously until 500 years (model "A", long-dashed) or 750 years (model "B", short-dashed) after the explosion. Note that the age-parameter in these models do not necessarily relate to the same age for SNR 0540-69.3 as it depends on the explosion energy, the envelope mass and the density structure. See text for further details.

2.7.2. Supernova ejecta absorption

Observations of SNR 0540-69.3 show that the remnant is oxygen-rich (Kirshner et al. 1989; Serafimovich et al. 2004), which means that the progenitor star probably was massive. Kirshner et al. (1989) suggest it to have had a mass similar to that of the SN 1987A progenitor, i.e., around 20 M$_\odot$, and the results of Serafimovich et al. (2004) show that a likely range is $15-22$ M$_\odot$. To check the importance of supernova ejecta for possible X-ray absorption, the well-studied SN 1987A therefore serves as a good template. We have used the mixed model 14E1 displayed in Figs. 2 and 6 in Blinnikov et al. (2000), which has ≈ 2 M$_\odot$ of pure oxygen spread out over the innermost ~ 5 M$_\odot$ of supernova ejecta. We assume that the post-explosion structure expands homologously. At an age of 1000 years after explosion, the hydrogen column density through the ejecta, from the center, is only $N_{\mathrm{HI}}(\mathrm{SN}) \approx 1.1 \times 10^{19}$ cm^{-2}, i.e., far less than even the MW contribution in the direction toward LMC. However, the very high metal content in the supernova ejecta, and its concentration toward the center of the ejecta, boosts the X-ray absorption at energies above 300 eV. Above the K-shell ionization edge of oxygen, i.e. at 600 eV, the cross section per hydrogen atom is ~ 40 times higher than for the MW absorption in MM83. Because $N_{\mathrm{HI}}(\mathrm{SN})$ scales with the time since explosion as $\propto t^{-2}$, a less evolved supernova remnant can make a significant contribution to the X-ray absorption of emission from the pulsar and its PWN.

The importance of the supernova ejecta is illustrated in Fig. 13. Here we have used the same value for $N_{\mathrm{HI}}(\mathrm{MW})$ as in Fig. 12, but lowered the LMC contribution to $N_{\mathrm{HI}}(\mathrm{LMC}) = 4.1 \times 10^{21}$ cm^{-2}. We have also included deabsorption due to supernova ejecta, assuming a homologously expanding SN 1987A at an age of 500 years (model "A", long-dashed) and 750 years (model "B", short-dashed). The increased oxygen column density compared to that in Fig. 12 makes it possible to retrieve the initial power-law spectrum above 0.6 keV for a supernova similar to SN 1987A at an age of 500 years, but it is also clear that a remnant with an age closer to the spin-down age of PSR B0540-69.3 will not contribute significantly to the X-ray absorption. Although the ejecta of SNR 0540-69.3 could expand more slowly than those of SN 1987A, could contain more oxygen (and/or having it more concentrated to the center), could have a clumpy and asymmetric structure (as is indicated for SN 1987A, Wang et al. 2002), or could have a lower age than the pulsar spin-down age, it seems that we have to stretch the parameters to claim that the X-ray absorption along the line of sight to the pulsar is largely affected by the supernova ejecta. A possible way to test this is to check the spatial variations of the X-ray absorption over the larger PWN. The low metal content of LMC, and the low MW foreground absorption, make such tests sensitive to any supernova ejecta contribution. X-ray spectral fits to data obtained with Chandra of the Crab pulsar have recently highlighted the importance of the abundance factor (Willingale et al. 2001; Weisskopf et al. 2003). Using various abundances it was found that the line of sight to the Crab is significantly underabundant in oxygen.

To summarize this section, it is evident that the X-ray spectral analysis of PSR B0540-69.3 needs a revision. Contrary to previous assumptions, the metal abundance of the X-ray absorbing gas must clearly be sub-solar, unless the supernova ejecta contribute significantly. The latter, however, appears to be less likely. While a full analysis of the X-ray spectrum, i.e., a detailed reduction of the Chandra data including various abundance combinations in XSPEC, is beyond the scope of this paper, we have argued that the power-law spectrum, which seems to be appropriate to use at energies above ~ 1 keV, may experience a depression below ~ 1 keV (cf. Sect. 3). This can be tested by how the X-ray spectrum connects to that in the optical. We will discuss that in Sect 3.

2.8. Extinction toward PSR B0540-69.3

As for the column density toward PSR B0540-69.3, the foreground optical extinction in the MW is well established. From the study of Staveley-Smith et al. (2003), the color excess in the direction toward PSR B0540-69.3 is $E(B - V)_{\mathrm{MW}} = 0.06$, and this agrees with the value found for SN 1987A (Scuderi et al. 1996) and that used by Gordon et al. (2003). The value used for the parameter R in these works is the standard value 3.1.

The extinction parameters $E(B - V)$ and $R(V)$ for LMC along the line of sight to SNR 0540-69.3 and the pulsar have not yet been investigated in detail in the same way as for SN 1987A (Scuderi et al. 1996). However, in Serafimovich et al. (2004) we studied SNR 0540-69.3 and H II regions close to it. The reduced spectra were analyzed using the total value $E(B - V)_{TOT} = 0.20$ and $R(V) = 3.1$, i.e., the same numbers we used in Sect. 2, and we found that the Hβ/Hγ/Hδ line ratios are in good agreement with Case B recombination theory (Baker & Menzel 1938; Hummer & Storey 1987). Allowing for higher extinction would boost Hγ and Hβ relative to Hβ causing a disagreement with the Case B theory, which for these lines normally explains the observations of supernova remnants well (e.g., Fesen & Hurford 1996).

Looking at the projected pulsar neighborhood, Gordon et al. (2003) obtain the average value $R(V)_{LMC} = 2.76 \pm 0.09$ for the LMC2 supershell, and it seems reasonable that this could be used also for PSR B0540-69.3. Out of the eight stars forming this average, six of them can accommodate the standard value of 3.1 within 1σ. The spread in $E(B - V)_{LMC}$ ranges between 0.12–0.24 (including 1σ errors), so the values we have used for PSR B0540-69.3 and its PWN in Sect. 2.4 and 2.5 seem reasonable also from this comparison. However, to check the effect of a different extinction curve on $E(B - V)$, and still being compatible with Case B line ratios for SNR 0540-69.3, we have compared k_{ext} (cf. Sect. 2.4) for the extinction used in Sect. 2.4 (we call that case "C1") to a case (called "C2") with $E(B - V)_{LMC} = 0.14$ ($R(V) = 2.76$, Gordon et al. 2003) and $E(B - V)_{MW} = 0.06$ ($R(V) = 3.1$, Cardelli et al. 1989). We formed the ratio $g(\lambda) = k_{ext}(\lambda)/k_{ext}(H\beta)$ for both cases, and found that $| g(\lambda)_{C1} - g(\lambda)_{C2} | /g(\lambda)_{C1}$ does not exceed 2% within the interval 2620–8480 Å. Only at the very blue end of the FOS spectrum of Hill et al. (1997), i.e., at $\approx$ 2500 Å, does the ratio approach 5%. This justifies the use of $E(B - V)_{LMC} = 0.14$ (assuming $E(B - V)_{MW} = 0.06$) regardless of whether we choose to use extinction combinations like C1 or C2. The absolute flux level of the dereddened spectrum of course depends on the exact value of $R(V)$ being used. Further direct extinction studies of the pulsar and its neighborhood in the UV and optical bands are needed to pin down the detailed extinction corrections. It seems, however, that the steep spectral slopes we obtain for the pulsar and its PWN in the optical in Sect. 2.4 and 2.5 cannot be corrected by some extreme reddening corrections as this is neither justified by our observations of the supernova remnant nor by the study by Gordon et al. for supposedly neighboring objects.

3. Discussion

3.1. Multiwavelength spectrum of PSR B0540-69.3

To connect the optical pulsar emission to the emission at other wavelengths, we have compiled results for the radio (Manchester et al. 1993a), X-ray (Kaaret et al. 2001;

de Plaa et al. 2003) and γ-ray (Thomson et al. 1994) spectral regions. The unabsorbed spectrum is displayed in Fig. 14. In comparison with previous compilations (e.g., Hirayama et al. 2002; de Plaa et al. 2003) the accuracy is significantly improved due to the new high spatial resolution data obtained in the optical with HST and in X-rays with Chandra. This reveals new features in the spectrum of the pulsar.

The optical and X-ray parts of the spectrum can be fitted with power-laws (for specific assumptions about the intervening extinction and photoelectric absorption discussed in Sect. 2.7 and 2.8), which would suggest a nonthermal nature of the emission in both domains, likely to be formed in the magnetosphere of the rotating neutron star. However, the connection between the emission in X-rays and in the optical seems far from trivial, especially if the slope for the optical spectrum derived from the archival HST/WFPC2/F336W data is correct (spectral indices and other emission parameters for PSR B0540-69.3, as well as for the Crab and Vela pulsars, in the optical and X-rays are presented in Table 8). The data for PSR B0540-69.3 suggest at least two spectral breaks between the optical and X-ray spectral bands. For a comparison, Fig. 14 also shows the multiwavelength spectrum of the total pulsed emission from the Crab pulsar (Kuiper et al. 2001; Sollerman 2003). For the Crab, it seems that a smooth turn-over can be possible (dotted line) between the X-ray band and the optical. This is in contrast to spectra of the middle-aged pulsars Vela and PSR B0656+14, whose optical fluxes are generally compatible with the low-frequency extrapolation of a power-law spectral tail for $E \gtrsim 1 - 2$ keV (Koptsevich et al. 2001; Shibanov et al. 2003).

In Sect. 2.7 we noted that PSR B0540-69.3 could have a non-powerlaw spectrum below $\sim 1 - 2$ keV, and inspired by this we tried to use the shape of the Crab optical/X-ray turn-over to fit the spectrum of PSR B0540-69.3. This, however, fails for the WFPC2/F336W band where the flux falls below such a fit. As we pointed out in Sect. 2.8, the depression in U is unlikely to be caused by insufficient dereddening; to reach the Crab pulsar spectral slope ($\alpha_\nu \approx -0.2$, cf. Table 8) one has to apply $E(B-V) \approx 0.55$, which is at least twice as high as the most likely value (cf. Sect. 2.8). Does this mean that PSR B0540-69.3 experiences a spectral dip in the F336W band? While future deep and well-calibrated data in U and UV should reveal this, we note that such an explanation is not far-fetched. As a matter of fact, the broad-band optical spectra of middle-aged pulsars (Vela, PSR B0656+14, and Geminga, cf. Shibanov et al. 2003) do show a dip in the U and B bands, which could indicate a multicomponent continuum spectrum, or the presence of unresolved emission/absorption features, possibly related to electron/ion cyclotron lines originating in the magnetospheres of the neutron stars (Mignani et al. 1998; Jacchia et al. 1999). If the depression in U is of more general character, the multiwavelength spectrum of PSR B0540-69.3 suggests a double break "knee" in the spectral region between the optical
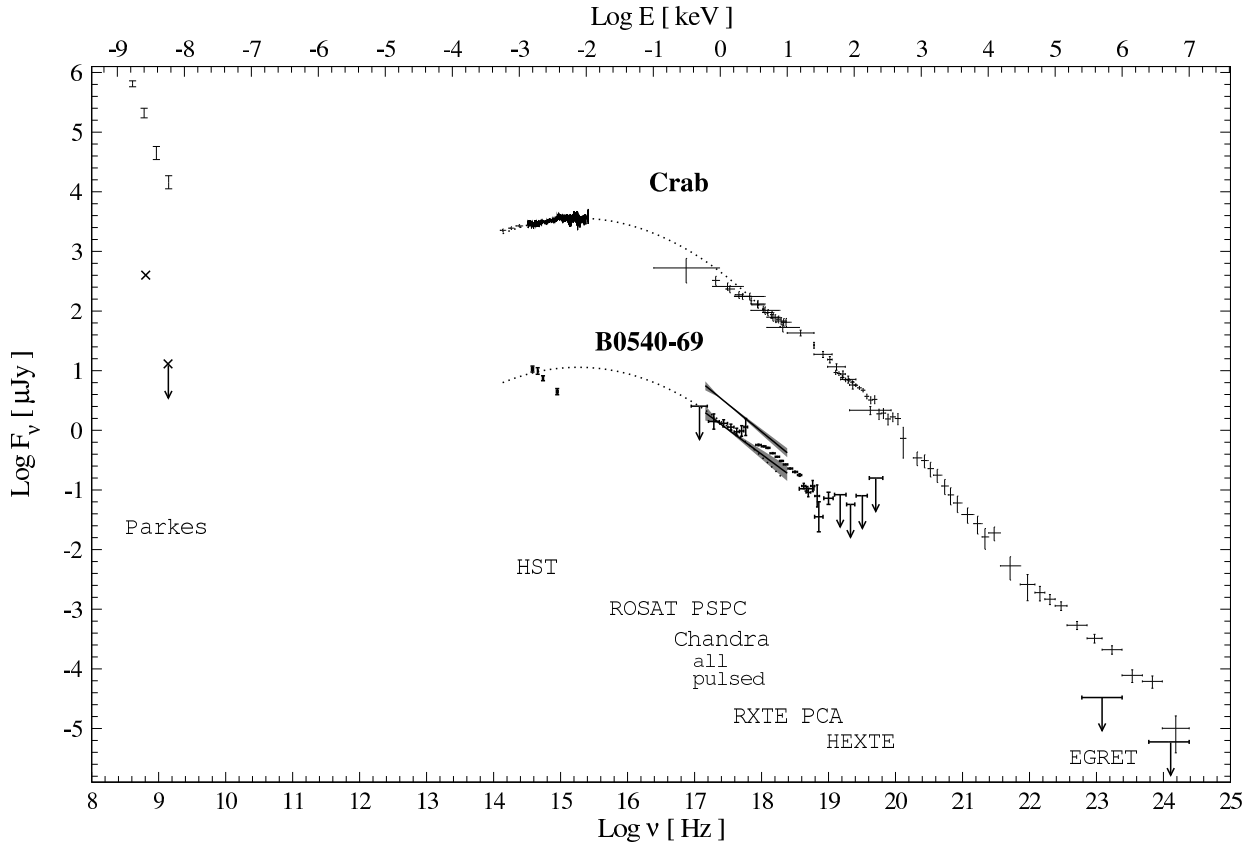
Fig. 14. Multiwavelength unabsorbed spectrum of PSR B0540-69.3. The data were obtained with the different telescopes and instruments marked in the plot. The optical data are from this paper. Phase-averaged (upper polygon) and pulsed (lower polygon) X-ray emission spectra with their uncertainties are shown for the 0.6 – 10 keV range (Kaaret et al. 2001). The pulsed emission spectra obtained with ROSAT and RXTE are from de Plaa et al. (2003), and the radio and γ-ray data are from Manchester et al. (1993a) and Thomson et al. (1994), respectively. All upper limits are defined at 3σ level. The unabsorbed spectrum of the total pulsed emission of the Crab pulsar is shown for comparison, where the high energy and optical data are from Kuiper et al. (2001) and Sollerman (2003), respectively. The dotted line for the Crab pulsar indicates a possible connection between the optical/X-ray regions through the EUV. The same line (shifted to overlap with the soft X-ray spectrum) is overlaid on the optical/X-ray region of PSR B0540-69.3. Note how the blue band fluxes of PSR B0540-69.3 undershoot by a factor of $\sim$3 compared to this overlay while it fits well in the X-ray band.

and soft X-ray bands. Observations in the UV and reanalysis of the Chandra X-ray data with accurate corrections for extinction and photoelectric absorption, as discussed in Sect. 2.7, will help us constrain the position of the breaks and to understand whether they are located just blueward of the U band and below 0.6 keV, or occur in the EUV range.

Taking into account the difference in distance to the Crab pulsar ($\sim$2 kpc) and PSR B0540-69.3 ($\sim$51 kpc), as well as the spectral energy distributions for both pulsars (see Fig. 14), we note that the overall intrinsic flux from PSR B0540-69.3 is almost as high as that from the Crab

pulsar in the radio (while its slope is possibly steeper in this range), but that it is $\sim$ 1.4 and $\sim$ 3 times higher in the optical and X-ray ranges, respectively. This is also shown in Table 8. At the same time, the spindown luminosity, $\dot{E}$, of PSR B0540-69.3 is $\sim$ 3 times lower than for the Crab. Therefore, the efficiency of producing nonthermal optical and X-ray photons in the magnetosphere of the rotating neutron star from its spindown power, $\eta = L/\dot{E}$, is a factor $\sim$ 4 and $\sim$ 10 higher for PSR B0540-69.3 in the optical and X-rays, respectively (Table 8). For a comparison we show also in Table 8 the parameters for the $\sim$ 10 times older Vela pulsar, which is much less luminous and a less effi-

Table 8. Comparison of the optical and X-ray spectral indices (α_ν^O, α_ν^X), luminosities (L^O, L^X), efficiencies (η^O, η^X), and a weighted ratio ($L^O \Delta E^X / L^X \Delta E^O$) of the two young pulsars, Crab and PSR B0540-69.3, and the older Vela pulsar. Here ΔE^O and ΔE^X are the energy intervals in the optical[a] and X-rays[b], respectively, used for the frequency integration to obtain L^O and L^X. Information on the period P, dynamical age τ, spindown luminosity $\dot{E}$, and distance d for each pulsar is included.

PSR	P ms	τ kyr	$\dot{E}$ 10^{37} erg s^{-1}	d kpc	α_ν^O	$L^{O,a}$ 10^{33} erg s^{-1}	η^O 10^{-5}	α_ν^X	$L^{X,b}$ 10^{36} erg s^{-1}	η^X 10^{-3}	$\frac{L^O \Delta E^X}{L^X \Delta E^O}$
Crab	33.49	1.24	46	2	-0.21[c]	7.9[c]	1.7	0.87[d]	1.0[d]	2.17	34.9
0540	50.2	1.66	15	51	1.07[e]	10.9[e]	7.3	0.83[d]	3.13[d]	21	15.5
Vela	89	11	0.69	0.29	0.25[f]	$7.0^f \times 10^{-5}$	1.0×10^{-3}	0.5[g]	$2.3^g \times 10^{-5}$	3.4×10^{-3}	13.5

[a] For the optical range 1.57–3.68 eV.
[b] For the X-ray range 0.6–10 keV.
[c] Using data from Sollerman (2003) for 1.57–3.68 eV.
[d] Kaaret et al. (2001); L^X rescaled to the 0.6–10 keV range.
[e] This paper.
[f] Using data from Shibanov et al. (2003).
[g] Pavlov et al. (2001a); L^X rescaled to the 0.6–10 keV range and $d = 0.29$ kpc.

cient optical and X-ray emitter, but still capable of powering a weak and less extended PWN around it. The Vela pulsar has also a peculiar optical spectrum in comparison with the Crab pulsar with a possible excess in the near-IR and a dip in the U band (Shibanov et al. 2003). Based on the available data it is not yet clear whether these spectral peculiarities in the pulsar optical emission do indicate a spectral evolution with pulsar age (PSR B0540-69.3 has a spin-down age which is $\sim$ 400 years higher than the Crab pulsar) or whether they are connected to the pulsar optical efficiency, or just reflects specific parameters (e.g., viewing angle and magnetic field geometry) of each pulsar. Detecting PSR B0540-69.3 in the near-IR would allow us to understand to which extent its spectrum is similar to that of the Vela pulsar and other middle-aged pulsars detected in the optical range. We also note that the ratio of optical to X-ray luminosity, weighted by the observed spectral ranges (cf. the last column in Table 8), is for PSR B0540-69.3 about half the value for the Crab pulsar, but comparable with that of the Vela pulsar.

3.2. Multiwavelength spectrum of the PWN

A compilation of our optical data for the PWN around PSR B0540-69.3 together with radio and X-ray data is shown as an unabsorbed multiwavelength spectrum in Fig 15. The spectrum suggests the same double knee connection between the optical and X-ray spectral parts as for the pulsar (cf. above). However, the assumed knee-breaks appear to be less pronounced than for the pulsar because the order of magnitude higher ratio for the intrinsic optical to X-ray flux for the PWN than for the pulsar. This is also reflected in the PWN luminosities presented in Table 9, where we have also collected information on the spectral indices and luminosities of the Crab and Vela PWNs. The smoothness of the knee in the PWN spectrum as compared to the pulsar spectrum may be explained by propagation effects of the relativistic particles generated in the pulsar magnetosphere and moving through the PWN. If the particle energy distribution function contains features which are reflected in the pulsar spectrum, these features should

become less pronounced due to such propagation effects. In Fig. 15, we also note a smaller difference between the radio and optical fluxes for the PWN, compared to for the pulsar, which may be also be caused by such propagation effects.

Unfortunately, there is no data of similar quality on the spatially averaged optical spectrum of the Crab PWN, but spectra of specific signatures of the Crab PWN (knots, wisps etc.) are significantly steeper than the pulsar spectrum (Sollerman 2003). On a larger scale, the continuum optical emission of the whole Crab Nebula, at $10''$ spatial resolution (Veron-Cetty & Woltjer 1993), shows a similar spectral behavior. In particular, a bright area roughly overlapping in position and morphology with the Crab X-ray PWN was resolved. Its spatially averaged spectrum is steeper than the spectrum of the pulsar. We see the same behavior for the whole PWN of PSR B0540-69.3 and for some parts of it (cf. Figs. 6 and 7), whereas the much fainter Vela PWN has not yet been detected in the optical (Mignani et al. 2003). However, some hints of specific structures in the Vela case, clearly detected in X-rays (Helfand et al. 2001; Pavlov et al. 2001), may have been detected also in the near-IR JH bands (Shibanov et al. 2003). There is no reliable spectral information on them and their identification still have to be confirmed by deeper observations both in the optical and IR.

The optical efficiency of the PWN of PSR B0540-69.3 is a factor of $\sim$ 30 higher than for the pulsar. This is markedly different from the situation in X-rays where the efficiency of the PWN is only $\sim$ 4 times higher than for the pulsar (Kaaret et al. 2001). If we assume that the bright optical areas of Veron-Cetty & Woltjer (1993) are associated with the the optical emission of the whole Crab PWN, we obtain a similar situation also for this pulsar with its $\sim$ 50 higher optical efficiency of the PWN compared to that of the pulsar, while the efficiency ratio is only a factor of 2–3 in X-rays. This may give a hint on the particle energy distribution responsible for the synchrotron emission of the PWN.

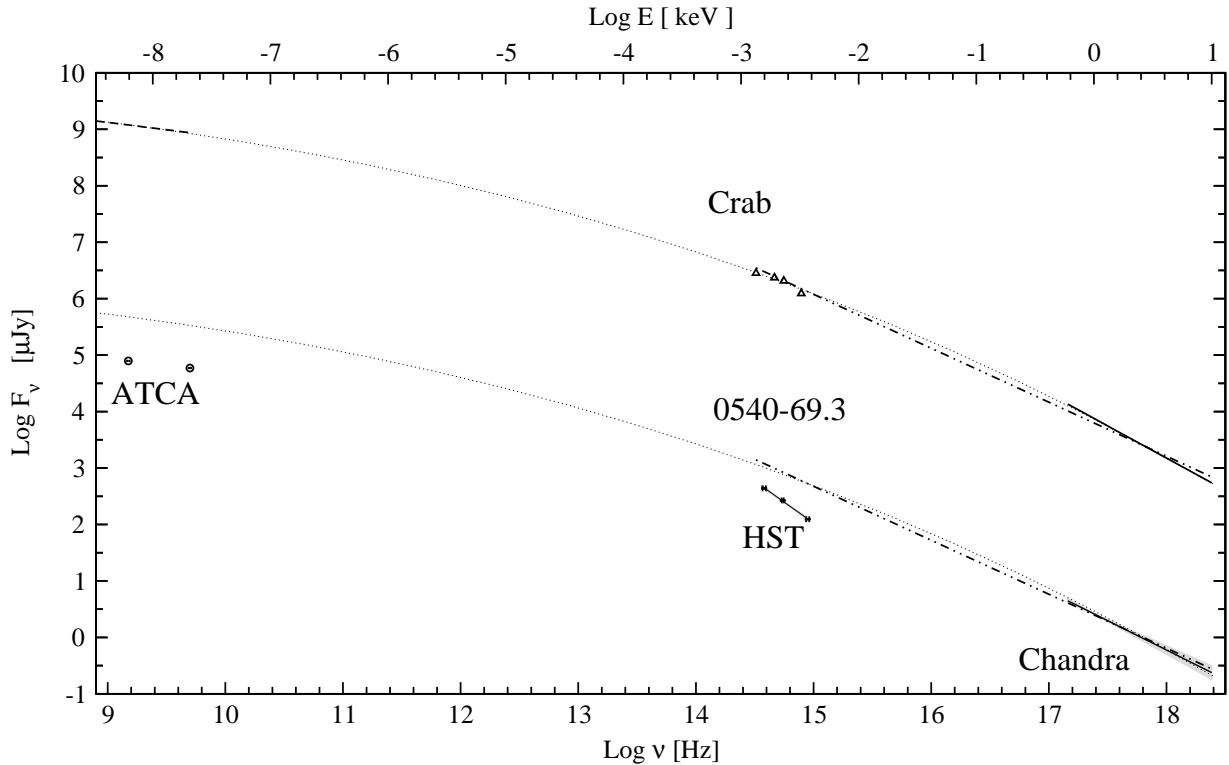To estimate the ratio of the efficiencies in the optical and X-rays we normalized the luminosity in each domain

Fig. 15. Spatially averaged multiwavelength spectrum of the PSR B0540-69.3 PWN obtained with the different telescopes indicated in the plot. The optical data are from the present work, whereas the radio and X-ray data are from Manchester et al. (1993b) and Kaaret et al. (2001), respectively. The filled regions (for the HST and Chandra data) show 1σ uncertainty regions around the best-fit power laws indicated by thick lines. We have also included similar data for the Crab PWN, where the data are from Velusamy et al. (1992), Veron-Cetty & Woltjer (1993) and Kaaret et al. (2001) for the radio, optical and X-ray bands, respectively. The dotted curved line is a cubic spline fit for the multiwavelength spectrum of the Crab PWN, and the dashed-dotted line is a linear fit for the optical/X-ray region of the Crab PWN. These fits have been shifted to the level of the X-ray emission of the PSR B0540-69.3 PWN for a comparison. Note how the fits overshoot for PSR B0540-69.3 in both the optical and the radio.

Table 9. Same as in Table 8 but for the PWNs of the same pulsars. Information on the PWN size and the ratios of the pulsar to PWN luminosities in the optical and X-rays for each pulsar is included.

PWN	size pc	α_ν^O	$L^{O,a}$ 10^{33} erg s^{-1}	η^O 10^{-5}	α_ν^X	$L^{X,b}$ 10^{36} erg s^{-1}	η^X 10^{-3}	$\frac{L^O \Delta E^X}{L^X \Delta E^O}$	L^O_{psr}/L^O_{pwn}	L^X_{psr}/L^X_{pwn}
Crab	1.5	0.92^c	4240^c	920	1.14^b	21.8^d	47.5	867	0.0017	0.046
0540	0.6–0.9	1.5^e	366^e	245	1.04^b	12^d	79.7	136	0.03	0.26
Vela	0.14	–	–	–	0.5^f	$6.8^d \times 10^{-4}$	9.8×10^{-2}	–	–	0.34

[a] For the optical range 1.57–3.68 eV.
[b] For the X-ray range 0.6–10 keV.
[c] Optical fluxes are taken from Veron-Cety & Woltjer (1993).
[d] Kaaret et al. (2001); L^X rescaled to the 0.6–10 keV range.
[e] This paper.
[f] From Pavlov et al. (2001b); L^X rescaled to the 0.6–10 keV range and $d = 0.29$ kpc.

to the respective energy range for which the luminosity was calculated. The ranges are 3370 – 7870 Å (i.e., 1.58–3.68 eV) and 0.6 – 10 keV. As seen in Tables 8 and 9, the normalized optical luminosity ($L^O \Delta E^X$ / $L^X \Delta E^O$, where the parameters are defined in Table 8) is ~ 16 and ~ 140 times higher than that in X-rays for the pulsar and its PWN, respectively. The inferred values for the Crab are even higher (~ 35 and ~ 870, respectively). This is natural

since the rotational loss of the Crab pulsar is ~ 3 times higher and its multiwavelength spectrum does not show a depression in the optical, as PSR B0540-69.3 appears to have.

The PWN of PSR B0540-69.3 has similar sizes in the optical (this paper) and in X-rays (Gotthelf & Wang 2000; Kaaret et al. 2001) and extends up to $4''$ away from the pulsar, which corresponds to ≈ 1

pc at 51 kpc. However, the brighter emission is confined to 0.6×0.9 pc (cf. Fig. 5). This is a factor of ~ 2 smaller than the size of the Crab PWN which has also similar sizes in the optical and in X-rays (Hester et al. 2002[8]). The smaller size of the PSR B0540-69.3 PWN is in rough agreement with the expected (e.g., Kennel & Coroniti 1984) PWN size scaling with pulsar spindown luminosity, $\propto \dot{E}^{0.5}$. A similar proportionality has been found from the comparison of the Crab and Vela PWNs (Helfand et al. 2001; Pavlov et al. 2001b).

The higher optical and X-ray efficiencies of PSR B0540-69.3, as compared with the Crab pulsar, are not reflected in a simple way in its PWN efficiencies. For instance, the X-ray efficiency of the PSR B0540-69.3 PWN is almost twice as high as that of the Crab PWN, while its optical efficiency is ~ 4 times lower than in the Crab case. The reason for this is unclear and may be explained either by the propagation effects discussed above, or by different pulsar environments, or a combination of these effects. The pulsar contribution to the total pulsar+nebula X-ray luminosity is 4.5%, 21%, and 25% for the PSR B0540-69.3, Crab, and Vela pulsars, respectively. The contribution is smaller in the optical and ranges from 0.17% for the Crab to 3% for PSR B0540-69.3. The Vela PWN has not been detected in the optical range, but we note that even for this much older and fainter pulsar, the PWN dominates the total X-ray luminosity, and that its contribution is comparable to that of PSR B0540-69.3, although $\dot{E}$ is an order of the magnitude smaller. This cannot be explained by a simple scaling with the spindown luminosity, as in case of the PWN sizes, and requires additional studies.

Our results do not reveal any significant variation of the spectral index over the torus and jet like structures of the PWN of PSR B0540-69.3, although a marginal inverse correlation between the spectral hardness and brightness cannot be excluded at 1.4σ level (cf. Fig. 10 and Sect. 2.5 for more details). No significant variation of the spectral index was also found in recent X-ray studies of the Crab PWN along its torus and the cores of the PWN jets (Mori et al. 2004). This suggests that for both these PWNs the energy spectra of the emitting electrons and positrons injected in these two different directions by the shocked pulsar wind are similar. This fact, as well as the similar sizes of the these parts of PWNs in the optical and X-rays suggest that the particle spectra in the bright, central parts of PWNs are not affected by synchrotron cooling. In the Crab case the spectral softening and hence the synchrotron losses become significant only in the faint outermost regions of the PWN detected in X-rays (Mori et al. 2004; Weisskopf et al. 2000) and in the UV/optical ranges (Scargle 1969; Veron-Cetty & Woltjer 1993; Hennessy et al. 1992). A similar dependence may be seen in the Vela PWN (Pavlov et al. 2001b). This imposes important constraints on the pulsar wind models.

---

[8] see also Chandra public images at chandra.harvard.edu/photo/2002/0052/0052_xray_opt.jpg

Deeper observations in the optical and X-rays are needed to study the faint outer regions of the PWN of PSR B0540-69.3, and to test the reality and magnitude of the inverse hardness/brightness correlation. We note a significant surface brightness asymmetry with the respect to the pulsar position along the major axis of the torus structure of the PWN of PSR B0540-69.3 seen in both the optical and in X-rays. This asymmetry can hardly be explained within the framework of axisymmetrical pulsar wind models by simply invoking Doppler boosting and relativistic aberration effects, as has been done for the near and far sides of the Crab PWN torus. The asymmetry is more likely to be caused by plasma instabilities in the internal parts of the pulsar wind flow, or by asymmetry of the SN ejecta. The latter is also discussed from another point of view in Sect. 3.3.

3.3. Proper motion and ejecta asymmetry

In Sect. 2.6 we found the indicative result that PSR B0540-69.3 has a high proper motion corresponding to 1190 ± 560 km s^{-1}, and that the direction is consistent with the pulsar moving along the southern jet axis. A pulsar velocity of ~ 1000 km s^{-1} is high, but not exceptional. In a recent VLA study of pulsar proper motions, Brisken et al. (2003) show that there is a relatively large fraction of pulsars which have velocities in excess of 500 km s^{-1}. Peng et al. (2003) quantify this number to be $\sim 16\%$.

Even if our results for the proper motion of PSR B0540-69.3 have only a 2σ significance, and a third epoch of HST imaging is needed to test whether or not PSR B0540-69.3 belongs to this high-velocity class of objects, we cannot avoid connecting the origin of the possibly large velocity of PSR B0540-69.3 to the origin of the significant redshift of the inner part of SNR 0540-69.3 which has been estimated to be several hundred km s^{-1} (Kirshner et al. 1989; Serafimovich et al. 2004). The most straightforward interpretation of this is that the 0540-69.3 system could be the result of a very asymmetric explosion.

Evidence of asymmetric supernova ejecta in core-collapse supernovae is abundant, and perhaps of specific interest for the 0540-69.3 system with its asymmetric inner ejecta structure (e.g., Kirshner et al. 1989), is that in general the asymmetry appears to increase with depth into the ejecta (see Akiyama et al. 2003 and references therein). The prime example is SN 1987A where the powering by radioactive nucleids in the center occurs along bipolar jets that are likely to be aligned with the rotational axis of the presupernova (Wang et al. 2002). Assuming that also the explosion in core-collapse supernovae itself could be jet-induced, Khoklov et al. (1999) find from 2D-modeling that pulsar kick velocities of ~ 1000 km s^{-1} can be achieved. The pulsar would move along the jet axis, consistent with our tentative finding for PSR B0540-69.3, but to reach a velocity as high as 1000 km s^{-1} a large difference in momentum between the two jets is required. As pointed out

by Lai (2000), it is not clear what could give rise to such a difference.

Lai et al. (2001) discuss various models how to produce large pulsar kick velocities in the context of the aligned spin axis and pulsar proper motion in Crab and Vela (cf. Sect. 2.6), and their discussion may now also apply to PSR B0540-69.3. The conclusion is that spin-kick alignment requires fast, perhaps close to break-up rotation, at the pulsar birth. There is observational evidence pointing in the same direction at least for the Crab pulsar (Atoyan 1999; Sollerman et al. 2001). We note that among the various models reviewed by Lai et al. (2001), the hydrodynamically driven kicks may face a problem in reproducing kick velocities of the order we infer for PSR B0540-69.3, and Fryer (2004) finds that even in his most asymmetric 3D-models of an exploding 15 $M_\odot$ star, the neutrino emission becomes asymmetrically emitted, thereby damping out the hydrodynamical pulsar kick. Fryer suggests that one way to obtain fast pulsars is to rely on them being produced by low-mass progenitors ($8 - 12$ $M_\odot$). This is, however, not a likely explanation for the 0540-69.3 system, which most probably originates from a ~ 20 $M_\odot$ progenitor. The recent models of Scheck et al. (2004) appear to be more successful in producing pulsars with high kick velocities. It could also be that models including rotation will alter the results of the hydrodynamically driven kick models (cf. Lai et al. 2001), perhaps providing a link to the results of Khoklov et al. (1999). Further observations of the 0540-69.3 system will show if it can add to Crab and Vela as a testbed for different kick scenarios.

References

Akiyama, S., Wheeler, J. C., Meier, D. L., Lichtenstadt, I. 2003, ApJ, 584, 954

Atoyan, A. M. 1999, A&A, 346, L49

Avila, G., Gero, R., & Beckers, J. M. 1997, in Optical Telescopes of Today and Tomorrow, SPIE 2871, ed. A. Ardeberg, 1135

Baker, J. G., Menzel, D. H. 1938, ApJ, 88, 52

Blair, W. P., Long, K. S., Wancura, O., et al. 1992, ApJ, 399, 611

Blinnikov, S. I., Lundqvist, P., Bartunov, O. S., et al. 2000, ApJ, 532, 1132

Bogovalov, S. V. & Khangoulyan, D. V. 2002, MNRAS, 305, 211

Boyd, P. T., van Citters, G. W., Dolan, K. G., et al. 1995, ApJ, 448, 365

Brisken, W. F., Fruchter, A. S., Goss, W. M., et al. 2003, AJ, 126, 3090

Caraveo, P. A., Bignami, G. F., Mereghetti, S., & Mombelli, M. 1992, ApJ, 395, L103

Caraveo, P. A., De Luca, A., Mignani, R. P., & Bignami, G. F. 2001, ApJ, 561, 930

Caraveo, P. A., Mignani, R. P., 1999 A&A, 344, 367

Caraveo, P. A., Mignani, R. P., De Luca, A., et al. 2000, in A decade of HST science, eds. Mario Livio et al. (Baltimore) 105, [astro-ph/0009035]

Cardelli, J. A., Clayton, G. C., Mathis, J. S. 1989, ApJ, 345, 245

Chanan, G. A., Helfand, D. J., & Reynolds, S. P. 1984, ApJ, 287, L23

Chevalier, R. A., & Kirshner, R. P. 1979, ApJ, 223, 154

Clark, D. H., Touhy, I. R., Long, K. S. 1982, ApJ, 255, 440

Carwford, F., Kaspi, V. M., Manchester, R. N., et al. 2001, ApJ, 553, 367

Cunto, W., Mendoza, C., Ochsenbein, F., & Zeippen, C. J. 1993, A&A, 275, L5

De Luca, A., Mignani, R. P., & Caraveo, P. A. 2000, A&A 354, 1011

Del Zanna, L., Amato, E., & Bucciantini, N. 2004, A&A, 421, 1063

de Plaa, J., Kuiper, L., Hermsen, W. 2003, A&A, 400, 1013

Dodson, R., Legge, D., Reynolds, J. E., & McCulloch, P. M. 2003, ApJ, 596, 1137

Dopita, M. A., & Tuohy, I. R., 1984 ApJ, 282, 135

Fesen, R. A., & Hurford, A. P. 1996, ApJS, 106, 563

Finley, J. P., Ögelman, H., Hasinger, G., et al. 1993, ApJ, 410, 323

Fryer, C. L. 2004, ApJ, 601, L175

Fukugita, M., Shimasaku, K., Ichikawa, T. 1995, PASP, 107, 945

Gordon, K. D., Clayton, G. C., Misselt, K. A., et al. 2003, ApJ 594, 279

Gotthelf, E. V. 2003, ApJ, 591, 361

Gotthelf, E. V., & Wang, Q. D. 2000, ApJ, 532, L117

Hamuy, M., Suntzeff, N. B., Heathcote, S. R. 1994, PASP, 106, 566

Hester, J., Mori, K., Burrows, D., et al. 2002, ApJ, 577, L49

Hill, R. J., Dolan, J. F., Bless, R. C., et al. 1997, ApJ, 486, L99

Hirayama, M., Nagase, F., Endo, T., et al. 2002, MNRAS, 333. 603

Hummer, D. G., & Storey, P. J. 1987, MNRAS, 224, 801

Hwang, U., Petre, R., Holt, S. S., & Szymkowiak, A. E. 2001, ApJ, 560, 742

Jacchia, A., de Luca, F., Lazzaro, E., et al. 1999, A&A, 347, 494

Jedrzejewski, R. I. 1987, MNRAS, 226, 747

Kaaret, P., Marshall, H. L., Aldcroft, T. L., et al. 2001, ApJ, 546, 1159

Kennel, C. F., & Coroniti, F. V. 1984, ApJ, 283, 694

Khokhlov, A. M., Höflich, P. A., Oran, E. S, et al. 1999, ApJ, 524, L107

Kirshner, R. P., Morse, J. A., Winkler, P. F., & Blair, W. P. 1989, ApJ, 342, 260

Komissarov, S. S., & Lubarsky, Y. 2004, MNRAS, 349, 779

Koptsevich, A., B., Pavlov, G. G., Zharikov, S. V., et al. 2001, A&A, 370, 1004

Korn, A. J., Keller, S. C., Kaufer, A., et al. 2002, A&A 385, 143

Kuiper, L., Hermsen, G., Cusumano, G., et al. 2001, A&A 378, 918

Lai, D. 2000, in Stellar Astrophysics, eds. L. S. Chang et al. (Kluwer) 127, [astro-ph/9912522]

Lai, D., Chernoff, D. F., & Cordes, J. M. 2001, ApJ, 549, 1111

Lundqvist, P., & Fransson, C. 1996, ApJ, 464, 924

MacAlpine, G. M., Lawrence, S. S., Sears, R. L., et al. 1996, ApJ, 463, 650

Manchester, R. N., Mar, D. P., Lyne, A. G., et al. 1993a, ApJ,, 403, L29

Manchester, R. N., Staveley-Smith, L., & Kesteven, M. J. 1993b, ApJ, 411, 756

Maran, S. P., Sonneborn, G., Pun, C. S. J., et al. 2000, ApJ, 545, 390

Mathewson, D. S., Dopita, M. A., Tuohy, I. R., & Ford, V. L. 1980, ApJ, 242, L73

Michael, E., McCray, R., Chevalier, R., et al. 2003, ApJ, 593, 809

Michael, E., Zhekov, S., McCray, R. 2002, ApJ, 574, 166

Middleditch, J., & Pennypacker, C. R. 1985, Nature, 313, 659

Middleditch, J., Pennypacker, C. R., Burns, M. S. 1987, ApJ, 315, 142

Mignani, R.P., Caraveo, P.A., Bignami, G.F. 1998, A&A, 332, L37

Mori, K., Burrows, D. N., Hester, J. J., et al. 2004, ApJ, 609, 186

Morrison, R., McCammon, D. 1983, ApJ, 270, 119

Morse, J. A. 2003, Rev.Mex.AA (Conf. Series), 15, 243

Oke, J. B., Gunn, J. E. 1983, ApJ, 266, 713

Panagia, N. 2004, in the Proceedings of IAU Colloquium 192: Supernovae (10 years of SN1993J), eds. J.M. Marcaide & K.W. Weiler (Springer Verlag), in press [astro-ph/0309416]

Pavlov, G. G., Kargaltsev, O. Y., Sandwal, D., et al. 2001a, ApJ, 552, 129

Pavlov, G. G., Zavlin, V. E., Sandwal, D., et al. 2001b, ApJ, 554, 189

Peng, Q., Zhang, L., Luo, X., & Chou, Ch. 2003, in Young neutron stars and their environment IAU Symp. 218, eds. F. Camilo & B. M. Gaensler (ASP Conference Proceedings) 17, [astro-ph/0309090]

Pont, M., & Shakeshaft, R. 1995, J. Phys. B, 28, L571

Samson, J. A. R., He, Z. X., Yin, L., & Haddad, G. N. 1994, J. Phys. B, 27, 887

Scheck, L., Plewa, T., Kifonidis, K., Janka, H.-Th., & Müller, E. 2004, in Proc. 12th Workshop on Nuclear Astrophysics, Ringberg Castle, in press [astro-ph/0404355]

Scuderi, S., Panagia, N., Gilmozzi, T., et al. 1996, ApJ, 465, 956.

Serafimovich, N. I., Lundqvist, P., Sollerman, J., & Shibanov, Yu. A. 2004, A&A, to be submitted

Seward, F. D., & Harnden, Jr. F. R. 1994, ApJ, 421, 581

Seward, F. D., Harnden, Jr. F. R., & Helfand, D. J. 1984, ApJ, 287, L19

Shibanov, Yu. A., Koptsevich, A. B., Lundqvist, P., Sollerman. J. 2003, A&A, 406, 645

Sollerman, J. 2003, A&A, 406, 639

Sollerman, J., Kozma, C., & Lundqvist, P. 2001, A&A, 366, 197

Sollerman, J., Lundqvist, P., Lindler, D., et al. 2000, ApJ, 537, 861

Staveley-Smith, L. 1994, PASAu, 11, 83

Staveley-Smith, L., Kim, S., Calabretta, M. R., et al. 2003, MNRAS, 339, 87

Stetson, P. B. 1987, PASP, 99, 191

Thomson, D. J., Arzoumanian, Z., Bertsch, D. L. et al. 1994, ApJ, 436, 229

van der Heyden, K. J., Paerels, F., Cottam, J., et al. 2001, A&A, 365, L254

Velusamy, T., Roshi, D., Venugopal, V. R., 1992, MNRAS, 255, 210

Veron-Cetty, M. P., & Woltjer, P. 1993, ApJ, 270, 370

Wang, L., Wheeler, J.C., Hoeflich, P., et al. 2002, ApJ, 579, 671

Weisskopf, M. C, O'Dell, S. L., Paerels, F., et al. 2003, ApJ, accepted [astro/ph0310332]

Willingale, R., Aschenbach, B., Griffiths, R.G., et al. 2001, A&A, 365, L212

Wilms, J., Allen, A. & McCray, R. 2000, ApJ, 542, 914